Thick discs, and an outflow, of dense gas in the nuclei of nearby Seyfert galaxies

Ming-Yi Lin,[1]★ R. I. Davies,[1]★ L. Burtscher,[1] A. Contursi,[1] R. Genzel,[1]
E. González-Alfonso,[2] J. Graciá-Carpio,[1] A. Janssen,[1] D. Lutz,[1] G. Orban de Xivry,[1]
D. Rosario,[1] A. Schnorr-Müller,[1] A. Sternberg,[3] E. Sturm[1] and L. Tacconi[1]

[1]*Max-Planck-Institut für extraterrestrische Physik, Postfach 1312, D-85741, Garching, Germany*
[2]*Universidad de Alcalá, Departamento de Física y Matemáticas, Campus Universitario, E-28871 Alcalá de Henares, Madrid, Spain*
[3]*Raymond and Beverly Sackler School of Physics and Astronomy, Tel Aviv University, Ramat Aviv 69978, Israel*

ABSTRACT

We discuss the dense molecular gas in central regions of nearby Seyfert galaxies, and report new arcsec resolution observations of HCN (1–0) and HCO$^+$ (1–0) for three objects. In NGC 3079, the lines show complex profiles as a result of self-absorption and saturated continuum absorption. H^{13}CN reveals the continuum absorption profile, with a peak close to the galaxy's systemic velocity that traces disc rotation, and a second feature with a blue wing extending to $-350\,\mathrm{km\,s^{-1}}$ that most likely traces a nuclear outflow. The morphological and spectral properties of the emission lines allow us to constrain the dense gas dynamics. We combine our kinematic analysis for these three objects, as well as another with archival data, with a previous comparable analysis of four other objects, to create a sample of eight Seyferts. In seven of these, the emission line kinematics imply thick disc structures on radial scales of $\sim$100 pc, suggesting such structures are a common occurrence. We find a relation between the circum-nuclear L_{HCN} and M_{dyn} that can be explained by a gas fraction of 10 per cent and a conversion factor $\alpha_{\mathrm{HCN}} \sim 10$ between gas mass and HCN luminosity. Finally, adopting a different perspective to probe the physical properties of the gas around active galactic nuclei, we report on an analysis of molecular line ratios which indicates that the clouds in this region are not self-gravitating.

Key words: galaxies: active – galaxies: ISM – galaxies: nuclei – galaxies: Seyfert – submillimetre: galaxies.

1 INTRODUCTION

The standard unification scheme for active galactic nuclei (AGN) proposes that the intrinsic properties of AGN are similar, and the disparity of observational properties arises from the different viewing angles with respect to an obscuring medium, resulting in type 1 and type 2 AGNs (Antonucci 1993; Urry & Padovani 1995). The reality may be more complex than this simple picture suggests (Netzer 2015), although, there is general agreement that the obscuring medium of gas and dust is a geometrically and optically thick toroidal structure (perhaps including an outflowing wind, e.g. Elitzur & Shlosman 2006) surrounding the AGN accretion disc, with its inner edge at the dust sublimation radius. Numerous observations confirm that there is dust at temperatures in the range 1000–1500 K (e.g. see Burtscher et al. 2015 and references

therein). And a variety of models for smooth (Pier & Krolik 1992; Granato & Danese 1994; Granato, Danese & Franceschini 1997; Schartmann et al. 2005; Fritz, Franceschini & Hatziminaoglou 2006) and clumpy (Krolik & Begelman 1988; Nenkova, Ivezić & Elitzur 2002; Hönig et al. 2006; Schartmann et al. 2008, 2014) media have been constructed to reproduce the spectral energy distribution (SED) at infrared wavelengths as well as the silicate feature at $\sim$10 µm (Schweitzer et al. 2008). However, a number of difficulties remain when applying these models to observations. Feltre et al. (2012) point out that in addition to the parameters describing the physical geometry, the assumptions built into the models can have a major impact on the resulting SED. And in the best-studied cases where interferometry can spatially resolve some of the structure, a component that is aligned along a direction consistent with an outflow appears to be responsible for much of the mid-infrared continuum (Tristram et al. 2014). Finally, in the context of the observations we present here, the outer edge of the torus is poorly defined for the majority of these models, because beyond a few tens

★ E-mail: mingyi@mpe.mpg.de (M-YL); davies@mpe.mpg.de (RID)

of parsecs, it contributes relatively little to the warm dust continuum against which the models are tested.

On radial scales of tens to a hundred parsecs, it is not clear whether one should still refer to the gas and dust structure as a torus or a (circum-)nuclear molecular disc. There have been claims that even on these scales the molecular disc is thick enough to have an impact on obscuration towards the AGN and so contributes to the observed difference between type 1 and type 2 AGN (Hicks et al. 2009; Sani et al. 2012); and hydrodynamical simulations suggest that turbulence injected via supernova from recent or ongoing star formation can puff up the disc to heights of $\sim$10 pc (Wada, Papadopoulos & Spaan 2009; Wada 2012). Spatially resolving molecular tracers on these scales in nearby AGN has become possible during the last decade, through the use of adaptive optics systems operating at near-infrared wavelengths and interferometers working in the millimetre regime.

Hicks et al. (2009) observed the $\sim$2000 K H_2 via the 2.12 μm 1–0 S(1) line. In most cases, the velocity dispersion (σ_{H2}) of this line exceeded its rotational velocity (v) on radial scales of $\sim$50 pc. Their conclusion was that the disc is relatively thick. The 2.12 μm line traces a small excited fraction of the H_2 mass that might have peculiar kinematics, so that kinematics from a tracer of the bulk of the molecular gas is desirable. Using the 3 mm HCN (1–0) line, Sani et al. (2012) modelled the emission as a rotating disc, and also found that a large intrinsic velocity dispersion (σ_{HCN}) was required to match the observations. Intriguingly, these results together, $\sigma_{H2} \sim 50$–100 km s^{-1} and $\sigma_{HCN} \sim 20$–40 km s^{-1}, suggest that the molecular gas is stratified with the warmest gas being the most turbulent and reaching to larger scaleheights while the denser clouds remain closer to the disc plane. Although several observations (e.g. Hicks et al. 2009 and Müller-Sánchez et al. 2013) have confirmed the presence of thick discs with $\sigma/v \sim 0.4$ on radial scales of $\sim$50 pc in some objects, it is not clear how the kinetic energy is continuously supplied in order to maintain the vertical structure of a rotating disc. One plausible explanation is that nuclear star formation can provide the necessary energy. Stellar radiation pressure (Thompson, Quataert & Murray 2005) is one option if there are sufficient OB stars and the interstellar medium (ISM) is optically thick. However, while some observations are consistent with ongoing star formation (Riffel et al. 2009; Esquej et al. 2014), others point more towards post-starburst populations (Cid Fernandes et al. 2004; Davies et al. 2007), and in some cases there is clear evidence that there cannot be ongoing star formation in the central tens of parsecs (Hicks et al. 2013). Alternatively, supernova explosions, associated even with a very modest star formation rate, are able to generate sufficient turbulence in the disc to yield $\sigma \sim 20$ km s^{-1} to radii of 25 pc (Wada & Norman 2002; Wada et al. 2009). A third possibility is that the gas flows induced by disc instabilities towards inner radii can also maintain a thick disc (Hopkins et al. 2012). Vollmer, Beckert & Davies (2008) also argued that the energy from inflowing gas could in principle be used to thicken the central disc.

The main purpose of this work is to model the intrinsic geometry (i.e. radial and height-scales) of the molecular disc in the central $\sim$100 pc around AGN, by using high-resolution HCN (1–0) and HCO$^+$ (1–0) observations. In addition, we use large velocity gradient (LVG) calculations for molecular line ratios to constrain the cloud properties in one of the objects, NGC 6951.

The HCN and HCO$^+$ molecules are ideal indicators of dense gas, since the higher dipole moments of their 1–0 rotational transitions can trace $\sim$100–500 times denser gas than the same rotational transitions of the CO molecule, and are sensitive to gas at $n_{H2} \sim 10^{4-5}$ cm^{-3} (Papadopoulos 2007). These molecules have

been successfully observed not only in dense star-forming regions but also in a number of Seyfert galaxies (Kohno 2005; Kohno et al. 2008; Krips et al. 2008; Sani et al. 2012), although, typically at resolutions of 5–20 arcsec. In the nuclear region of Seyfert galaxies, HCN (1–0) and HCO$^+$ (1–0) can be excited either by UV light from the accretion disc or X-ray radiation from the corona (Sternberg & Dalgarno 1995; Lepp & Dalgarno 1996; Maloney, Hollenbach & Tielens 1996; Boger & Sternberg 2005; Meijerink & Spaans 2005; Meijerink, Spaans & Israel 2007, and the references therein).

This paper is organized as follows. The HCN (1–0) and HCO$^+$ (1–0) observations of NGC 3079, NGC 6764, and NGC 5033 are described in Section 2. We present the observed molecular gas distribution and kinematics for each galaxy in Section 3. We apply a simple dynamical model to the emission lines in Section 4, and in Section 5 use the H^{13}CN (1–0) absorption to estimate the column density of the disc in NGC 3079. Section 6 brings in data from the literature to explore the relation between HCN luminosity and dynamical mass for a sample of eight objects with high spatial resolution HCN observations. Finally, Section 7 looks more closely at the cloud properties for one specific object NGC 6951 where data for suitable transitions are available. We summarize our conclusions in Section 8.

2 OBSERVATIONS

We used the six 15-m antennas of the Institut de Radiostronomie Millimétrique (IRAM) Plateau de Bure interferometer (PdBI) to observe NGC 3079, NGC 6764, and NGC 5033 at 88 GHz (3 mm) with the WideX correlator in the extended A configuration. The basic calibration steps of three galaxies were done with the CLIC software. The observations for the individual galaxies are described below and summarized in Table 1.

Observations of NGC 3079 (systemic velocity 1147 km s^{-1} and inclination 77°; Koda et al. 2002) were carried out on 2011 January 19 for programme UD8A. The receiver band was centred at 87.55 GHz with its 3.6 GHz bandwidth covered all features from HCO$^+$ (1–0) at 89.2 GHz to H^{13}CN (1–0) at 86.3 GHz (rest frequencies). During the 5.5 h track, the average antenna efficiency was 22.6 Jy K^{-1}, and the precipitable water vapour (pwv) improved during the track from 2–4 mm to $<$2 mm. The calibrators include 3C273, 0923+392, 0954+556, and MWC349. After data reduction, the synthesized beam at 89 GHz was 1.2 × 0.9 arcsec at position angle (PA) 167°. The data were binned to a spectral resolution of 5 MHz corresponding to a channel width of 17 km s^{-1}, yielding a root mean square uncertainty of 0.37 mJy beam^{-1}. This was chosen in order to balance signal to noise with high spectral resolution, since some of the absorption features are much narrower than the emission lines. Images of the channels were reconstructed with a pixel size of 0.2 arcsec. We adopt a distance to NGC 3079 of 19.7 Mpc, for which 1 arcsec corresponds to 85 pc.

NGC 6764 was also observed on 2011 January 19, after NGC 3079, with the receiver band centred at 87.15 GHz. This setting was based on the systemic velocity of 2416 km s^{-1} used by Hota & Saikia (2006), who found deep H I absorption on the location of the nucleus at a velocity of 2426 km s^{-1} consistent with that velocity. However, the profiles of both the HCN (1–0) and HCO$^+$ (1–0) lines in our data are centred at 2468 km s^{-1} (each differing by only 10 km s^{-1} from that mean). This implies that the H I may be outflowing, a phenomenon that has been observed in a number of galaxies (see Morganti 2012 for a review), for example in the Seyfert IC 5063 the H I absorption is blueshifted with respect to the H I emission with velocities comparable to a blue wing in the CO

Table 1. Summary of observations for the three Seyfert galaxies. (1) Source name; (2) Beam size; (3) Beam position angle; (4) Channel width; (5) Noise per beam; (6) Distance; (7) Physical scale of 1 arcsec.

Source	Beam size	PA (°)	Channel resolution (km s^{-1})	Noise (mJy beam^{-1} ch^{-1})	Distance (Mpc)	Scale (pc arcsec^{-1})
NGC 3079	1.17 arcsec × 0.94 arcsec	167	17.1	0.37	20	85
NGC 6764	1.16 arcsec × 0.78 arcsec	13	34.4	0.29	32	150
NGC 5033	1.13 arcsec × 0.83 arcsec	38	34.2	0.31	19	73

Table 2. Summary of the continuum properties for the three targets: (1) Source name; (2) Flux density; (3) The observed FWHM of the major and minor axes; (4) Position angle (east of north).

Source	Flux density (mJy)	Major × Minor axis (arcsec^2)	PA (°)
NGC 3079	27.8 ± 0.15	1.19 ± 0.01 × 1.06 ± 0.01	176 ± 1
NGC 6764	0.6 ± 0.06	1.04 ± 0.05 × 0.82 ± 0.04	8 ± 2
NGC 5033	0.7 ± 0.08	1.01 ± 0.04 × 0.79 ± 0.03	41 ± 2

(2–1) line (Morganti et al. 2007, 2015). In our analysis, we use 2468 km s^{-1} as the systemic velocity for NGC 6764. We also adopt an inclination of 62° based on CO (1–0) kinematics (Leon et al. 2007). During the 4.9 h track, the average antenna efficiency was 22.9 Jy K^{-1}, and the pwv was <1 mm. The calibrators include MWC349, 1954+513, 1739+522, 1749+096, and 1823+568. The synthesized beam at 89 GHz in the processed data was 1.2 arcsec × 0.8 arcsec at a PA of 13°. The data were spectrally binned to 10 MHz, corresponding to a channel width of 34 km s^{-1} and a root mean square uncertainty of 0.29 mJy beam^{-1}. The channel binning is coarser than for NGC 3079 but sufficient to sample the velocity width of the emission lines. In order to fit disc models, the data were converted to an image plane with a pixel size of 0.3 arcsec. We adopt a distance to NGC 6764 of 31.7 Mpc, for which 1 arcsec corresponds to 150 pc.

Observations of NGC 5033 (systemic velocity 875 km s^{-1}, Huchra, Geller & Corwin 1995; inclination 68°, Thean et al. 1997; Kohno et al. 2003) were conducted over two nights on 2011 January 26 and 28, with tracks of 3.1 and 3.9 h, respectively. The receiver band was centred at 87.60 GHz. The average antenna efficiency of 22.7 Jy K^{-1}, with pwv <1 mm on the first night and <3 mm on the second night except near the end when it increased slightly. The calibrators include 3C273, MWC349, 1308+326, and 0355+508. After data reduction, the synthesized beam size at 89 GHz was 1.1 arcsec × 0.8 arcsec at a PA of 38°. The reconstructed data for NGC 5033 share the same spectral binning and pixel size as NGC 6764, and have a root mean square uncertainty of 0.31 mJy beam^{-1}. We adopt a distance to NGC 5033 of 18.7 Mpc, for which 1 arcsec corresponds to 73 pc.

We also make use of HCN (1–0) data for NGC 7469 presented in Davies, Tacconi & Genzel (2004), which have a beam size of 2.0 arcsec. We adopt a distance of 58 Mpc and an inclination of 45°.

3 GAS DISTRIBUTION AND KINEMATICS

We begin this section by describing the general properties of the three galaxies, and then present the details for each individual source in the following subsections. HCN (1–0) at 88.63 GHz, and HCO$^+$ (1–0) at 89.19 GHz were detected in all galaxies.

In every case, the 3 mm continuum (spectrally integrated over channels that are free from molecular transitions) is seen as a single compact source. Since the major and minor axes, and the PA, are very close to those of the beam, the continuum appears to be spatially

unresolved. The flux density and morphology of the continuum sources are derived from line-free regions of the spectrum, and are given in Table 2.

In contrast, the HCN (1–0) and HCO$^+$ (1–0) emission line morphologies are spatially extended, although by not more than a few arcsec. We define the centre from the continuum image, and extract an integrated spectrum in a 3 arcsec diameter aperture around that. The flux density of the emission lines is derived from this by summing overall channels across the spectral line profile. It is important to note that for NGC 3079, HCN (1–0) and HCO$^+$ (1–0), both show a clear P-Cygni shape, with absorption cutting through the emission line profile. For both NGC 6764 and NGC 5033, the lines are seen in emission only. As for the continuum, the morphology of the molecular lines is quantified by fitting a two-dimensional Gaussian function to the line map. In addition, we have measured the centres of the emission summed over red channels and blue channels separately (the velocity ranges are from line centre to ±350–480 km s^{-1} depending on the line and object; specific ranges are given in the following subsections), in order to derive their relative separation and PA. The observed properties of the molecular emission lines are summarized in Table 3.

3.1 NGC 3079

The 3 mm continuum is displayed in the left-hand panel of Fig. 1. A Gaussian fit indicates full width at half-maximum (FWHM) of 1.19 arcsec × 1.04 arcsec at a PA of 176°. These are comparable to the beam size, indicating that the source is not spatially resolved, and has an intrinsic size <0.5 arcsec. Because of the absorption features we have observed, the origin of the 3 mm continuum is an important issue. Maps of the radio continuum at 5–22 GHz and at resolutions to <1 mas (Trotter et al. 1998; Kondratko et al. 2005; Middelberg et al. 2007) demonstrate that it is dominated by regions that are 1–3 pc from the dynamical centre as defined by Trotter et al. (1998). Fig. 2 shows the radio to infrared SED for NGC 3079 and indicates that the two radio lobes A and B are likely to dominate also the 3 mm continuum. In 2001, the sum of the flux densities of these two components (68 mJy) at 22 GHz was equal to the total radio continuum integrated over arcsec scales; and there is some evidence that they have continued to brighten at 22 GHz in subsequent years (Middelberg et al. 2007). The discussion below is based on the conclusion that the 3 mm continuum, which is clearly

Table 3. The observed properties of molecular emission for three targets: (1) Source name; (2) Molecule; (3) Flux[a]; (4) Observed FWHM of major and minor axes; (5) Position angle (east of north); (6) Separation between centres of red and blue channel maps; (7) Position angle between centres of the red and blue channel maps; (8) Spectral FWHM of line (3 arcsec aperture).

Source	Line	Flux (Jy km s^{-1})	Major × minor axis (arcsec^2)	PA (°)	b/r sep. (arcsec)	PA$_{b/r}$ (°)	Line width (km s^{-1})
NGC 3079	HCN	8.20[b]	(2.94 ± 0.14) × (1.44 ± 0.06)	167 ± 2	1.51 ± 0.02	−21 ± 2	360[c]
	HCO+	4.78[b]	strong absorption	strong absorption	1.70 ± 0.04	−20 ± 2	−
NGC 7469	HCN	5.30 ± 0.10	(3.43 ± 0.10) × (2.73 ± 0.08)	78 ± 15	1.14 ± 0.04	118 ± 2	236 ± 9
NGC 6764	HCN	1.92 ± 0.11	(1.71 ± 0.14) × (1.31 ± 0.09)	−54 ± 25	0.82 ± 0.11	−87 ± 7	214 ± 17
	HCO+	2.28 ± 0.09	(1.69 ± 0.11) × (1.21 ± 0.06)	−66 ± 7	1.04 ± 0.11	−85 ± 8	203 ± 16
NGC 5033	HCN	1.16 ± 0.14	(1.97 ± 0.30) × (1.09 ± 0.13)	−17 ± 10	1.06 ± 0.15	158 ± 19	181 ± 32
	HCO+	0.71 ± 0.14	(1.76 ± 0.40) × (1.22 ± 0.20)	52 ± 67	0.99 ± 0.56	184 ± 51	185 ± 71

Notes. [a]These are given in a 3 arcsec aperture, except for NGC 3079 where we have used a 5 arcsec aperture.
[b]Fluxes are integrated across the observed line profile above the continuum level. Applying corrections in a simple way as illustrated by the blue line in the right-hand panel of Fig. 4 yields fluxes for HCN (1–0) of 16.1 Jy km s^{-1} when accounting for only the continuum absorption, and 18.7 Jy km s^{-1} when also accounting for the self-absorption. The equivalent corrected fluxes for the HCO+ (1–0) line are 13.3 and 19.5 Jy km s^{-1}.
[c]Estimated intrinsic line width after correcting for continuum absorption and self-absorption (i.e. it corresponds to the blue Gaussian line profile in the right-hand panel of Fig. 4). We have adopted an uncertainty of 20 km s^{-1} typical of the other line width measurements.

non-thermal, is dominated by the radio components A and B, rather than by any emission from the dynamical centre.

The maps of HCN (1–0) and HCO+ (1–0) are presented in the middle and right-hand panels of Fig. 1. The grey-scale image indicates the full line distribution, while the red and blue contours represent the distribution of integrated red channels and blue channels of the emission lines. For NGC 3079, the ranges for both lines extend from line centre to approximately −420 and +480 km s^{-1}. The spatial separation and PA of the centroids of these two channels are ∼1.5 arcsec and 21°.

The absorption is clearly visible in the central region for both molecules. In particular, HCO+ has stronger absorption than HCN. While this means we cannot reliably fit a Gaussian to the HCO+ emission, it is still possible to do so on the HCN map. The resulting FWHM is 2.94 arcsec × 1.44 arcsec and PA is 167° (Table 3).

Panel (a) of Fig. 3 shows the integrated spectrum of NGC 3079. Although a clear P-Cygni line profile is apparent for the HCN (1–0) and HCO+ (1–0) line due to the strong emission of these lines, blueshifted absorption with two or more components dominates the profile of other lines where an emission component is weak or absent. These include H^{13}CN (1–0) at 86.34 GHz, H^{13}CO+ (1–0) at 86.75 GHz, SiO (2–1) at 86.85 GHz, and HN^{13}C (1–0) at 87.09 GHz (rest frequencies). The narrow absorption peak closest to systemic velocity is strongly absorbed, reaching maximum depths of 87 per cent, 56 per cent, 71 per cent, and 42 per cent of the continuum level respectively. The absorption profiles show a second narrow peak with a blueshifted tail (that may itself contain several subcomponents) that reaches to −350 km s^{-1}. The absorption that we have identified as C$_2$H at 87.3–87.4 GHz is at relatively low signal to noise and is likely to include features from several of the hyperfine transitions (Gottlieb, Gottlieb & Thaddeus 1983; Schöier et al. 2005). We therefore exclude this from our analysis.

Panel (b) of Fig. 3 shows the double-peaked absorption of H^{13}CN (1–0). While there may be substructure within the full velocity extent of the absorption, for our analysis, and discussion of the implications, in Section 5, we consider this as only two features. The reason is that we prefer to interpret the absorption in the context of its physical origin, and we argue in Section 5 that the narrow peak closer to systemic is due to absorption by the nuclear disc, while the more blueshifted component, as well as its high-velocity tail, originates in absorption by outflowing gas clouds. We note also that the absorption profile of the H^{13}CN (1–0) line is very different to

that of HCN (1–0). This is for two reasons: it is not saturated while, as discussed below, the HCN (1–0) absorption is strongly saturated [and as a result, one cannot use the H^{13}CN (1–0) profile to correct for the HCN (1–0) absorption]; and because any associated line emission is very weak, the absorption profile is not partially filled, as is the case for the HCN (1–0) line. These issues are discussed in detail below in Section 3.1.1.

There are few reports of HCN (1–0) or HCO+ (1–0) absorption in the literature. This could be because most mm spectra of galaxies are still from single dish rather than interferometric observations and, as we discuss below in Section 3.1.2, extended low-intensity emission will tend to fill in any absorption of a weak continuum. The two cases of which we are aware, blueshifted HCO+ (4–3) absorption in Arp 220 (Sakamoto et al. 2009) and redshifted HCN (3–2) and HCO+ (3–2) absorption in IC 860 (Aalto et al. 2015), were both obtained with sub-arcsec resolution interferometric observations.

3.1.1 Correction for absorption

The observed (i.e. without correcting for the absorption) flux of HCN (1–0) is 8.20 Jy km s^{-1} and of HCO+ (1–0) is 4.78 Jy km s^{-1}, both in 5 arcsec apertures to cover the full extent of the observed emission. In order to estimate a correction for the absorption, we fit a Gaussian function to the emission profile, including an additional constraint that the intrinsic absorption as measured from the continuum level cannot go below zero. This approach is motivated under the assumption that the absorption and emission are effectively independent: the absorption at any given velocity occurs over a very small area (defined by the size and location of continuum sources) while the emission is integrated over the full extent of that isovelocity contour across the molecular disc (note that we did not require that the centre of the symmetric emission should be exactly at the systemic velocity of molecular line because the line emission may not be symmetric about the centre of the rotating disc), and partially fills the absorption. The best-fitting profile is shown as a solid green line in the left-hand panel of Fig. 4, where the black solid line traces the observed HCN (1–0) profile. The difference between these is represented by the dashed green line, which traces the intrinsic absorption profile from the continuum level. Its truncated shape indicates that the HCN (1–0) line is strongly saturated. The strong red wing of the observed emission profile, and the constraint on the depth of the intrinsic absorption, result in a fit
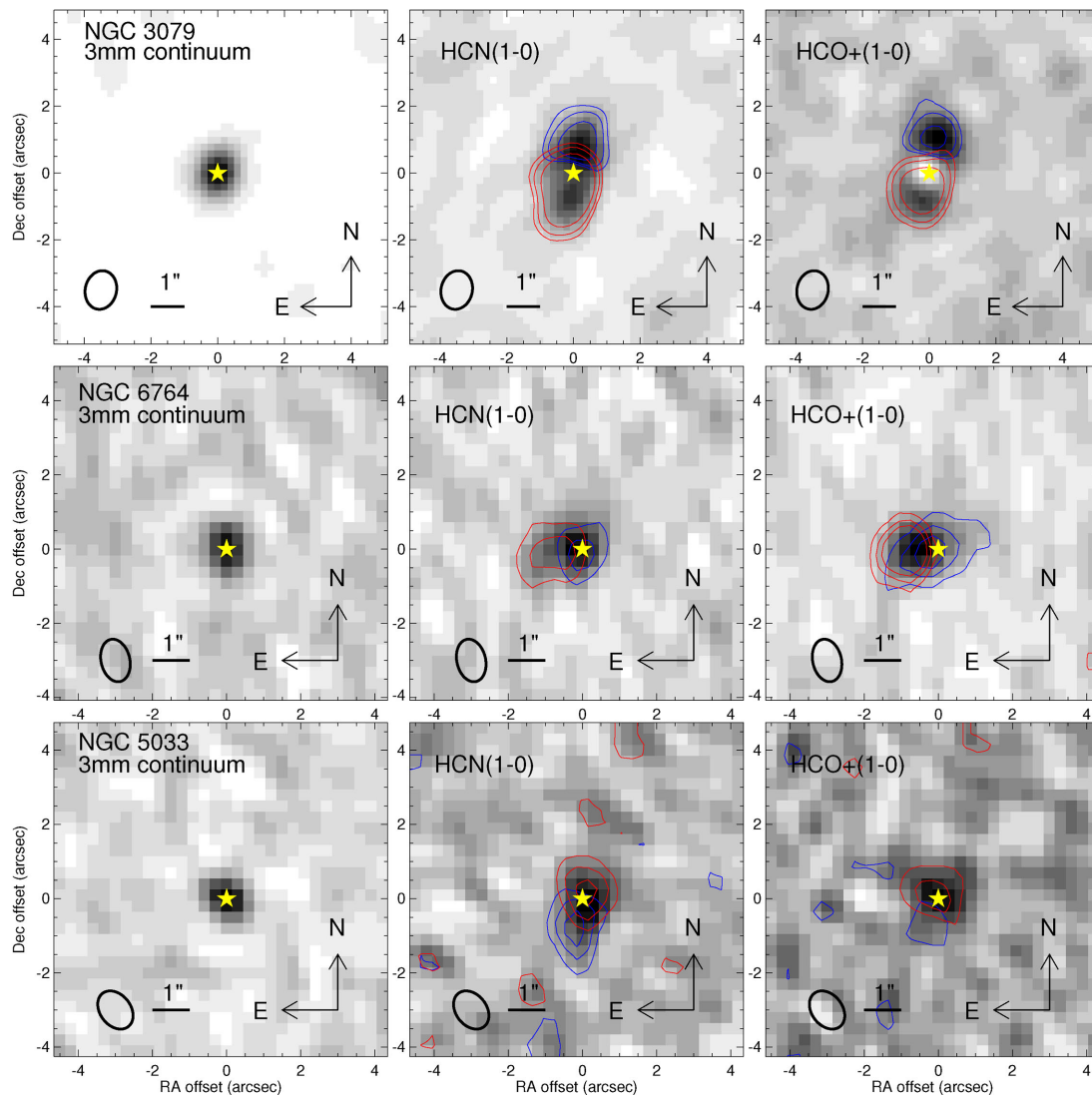
Figure 1. The 3 mm continuum (left-hand panels), integrated HCN (1–0) (middle panels), and integrated HCO$^+$ (1–0) (right-hand panels) emission maps of NGC 3079 (top row), NGC 6764 (middle row), and NGC 5033 (bottom row). In each panel, the peak position of 3 mm continuum is marked as a yellow star and the synthesized beam is drawn as an ellipse. The 3 mm continuum has been subtracted from HCN and HCO$^+$ maps. The blue and red contours represent the distribution of integrated blue and red channels of the emission lines, and are easily spatially resolved. For NGC 3079, the map is centred at 10 01 57.80 + 55 40 47.2 (J2000). The absorption appears as a 'hole' in the central region, more clearly in the HCO$^+$ map due to the stronger absorption of that line. Blue and red contours are drawn at levels of 2σ, 3σ, and 5σ. Note that while the absorption is blueshifted, in these images it appears to be occurring within the red contours. As becomes clear in Fig. 8, this is because the blueshifted emission is filling in the absorption and therefore remains below the continuum level, so the blue contours do not extend over that region. For NGC 6764, the map is centred at 19 08 16.38 + 50 55 59.4 (J2000), and blue and red contours are drawn at levels of 0.5σ, 1σ, and 1.5σ. For NGC 5033, the map is centred at 13 13 27.47 + 36 35 37.9 (J2000), and blue and red contours are drawn at levels of 0.5σ, 1σ, and 1.5σ.

whose peak is offset by $\sim$100 km s^{-1} from systemic and which underestimates the blue wing of the emission line profile. In addition, the continuum absorption lacks the blue wing seen in the H^{13}CN profile. To avoid these discrepancies, we have made a second reconstruction, which is shown in the right-hand panel of Fig. 4. For this, we have added the requirement that the intrinsic Gaussian line profile (dotted blue line) should be centred at the systemic velocity. We find that, because the continuum absorption (dashed blue line) cannot go below zero, the reconstructed line profile (solid blue line) cannot be Gaussian – noting that the sum of these two must match the observed profile. Instead, in comparison to the Gaussian, it shows absorption that is roughly symmetric and centred approx-

imately at the systemic velocity. We interpret this to mean that the HCN (1–0) line is self-absorbed. Self-absorption in an HCN (1–0) line has been reported in IC 860 and Arp 220 W by Aalto et al. (2015) in the context of the compact obscured nuclei of luminous and ultraluminous infrared galaxies. It has also been reported in the CO 2–1 and CO 6–5 lines in Arp 220 by Engel et al. (2011) and Rangwala et al. (2015), respectively. In the case of NGC 3079, we suggest that it is occurring because the galaxy is inclined so close to edge-on. As such, there is plenty of cool gas in the disc of the galaxy along the line of sight, that could absorb the line emission. From the depth of the self-absorption, we estimate that a total column of $N_{\text{HCN}} = 1.4 \times 10^{14}$ cm^{-2} is needed to produce it, corresponding to
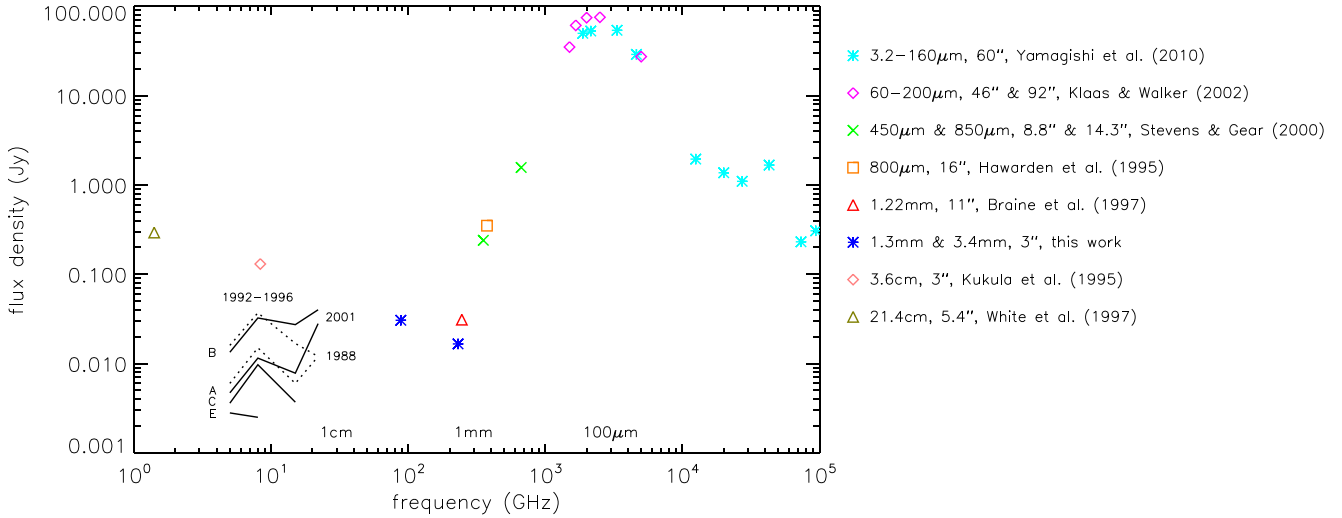
Figure 2. Radio to infrared spectral energy distribution (SED) for NGC 3079 as well as the interferometric mm-to-cm SED for the four radio-emitting knots. Knots A and C are associated with approaching jet to the south-east (SE) that is in front of the nuclear disc; while knot B is associated with the receding jet to the north-west (NW) that is behind the disc. The SED shows that the continuum longward of 1 mm is non-thermal, and that the 3 mm continuum in the central few arcsec is likely dominated by the two radio knots A and B. References for photometry: 3.2–160 μm (60 arcsec apertures) from Yamagishi et al. (2010); 60–200 μm (46 and 92 arcsec apertures) from Klaas & Walker (2002); 450 μm (8.8 arcsec) and 850 μm (14.3 arcsec) from Stevens & Gear (2000); 800 μm (16 arcsec) from Hawarden et al. (1995); 1.22 mm (11 arcsec) from Braine et al. (1997); 1.3 and 3.4 mm (3 arcsec aperture) from this work; 3.6 cm (3 arcsec beam) from Kukula et al. (1995); 21.4 cm (5.4 arcsec beam) from White et al. (1997). The interferometric radio continuum measurements of components A, B, C, and E with beam sizes of 0.3–8 mas are from Trotter et al. (1998) and Kondratko, Greenhill & Moran (2005).
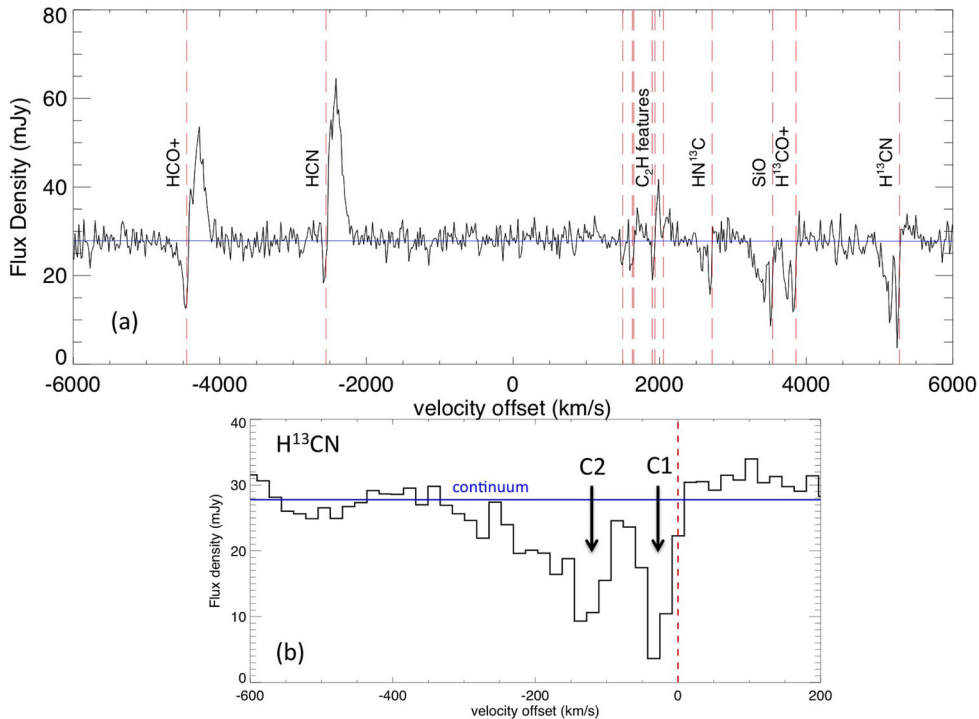

Figure 3. Panel (a): the spectrum of NGC 3079 integrated within a 3 arcsec aperture (velocity offset is with respect to the band centre). Transitions of $H^{12}CO^+$ (1–0), $H^{12}CN$ (1–0), $HN^{13}C$ (1–0), SiO (2–1), $H^{13}CO^+$ (1–0), and $H^{13}CN$ (1–0) are detected, as well as hyperfine transitions of C_2H (1–0). The blue solid line is a constant representing the 3 mm continuum. The red dash lines indicate the velocity offsets of each molecular transition with respect to the galaxy systematic velocity of $1147\,km\,s^{-1}$. Panel (b): the complex absorption of the $H^{13}CN$ (1–0) transition (in a 3arcsec aperture). Velocity offsets are given with respect to its systemic, denoted by the dashed red line. The deepest absorption is labelled as 'C1' and the broader absorption is labelled as 'C2'. Note that both absorption features are blueshifted.
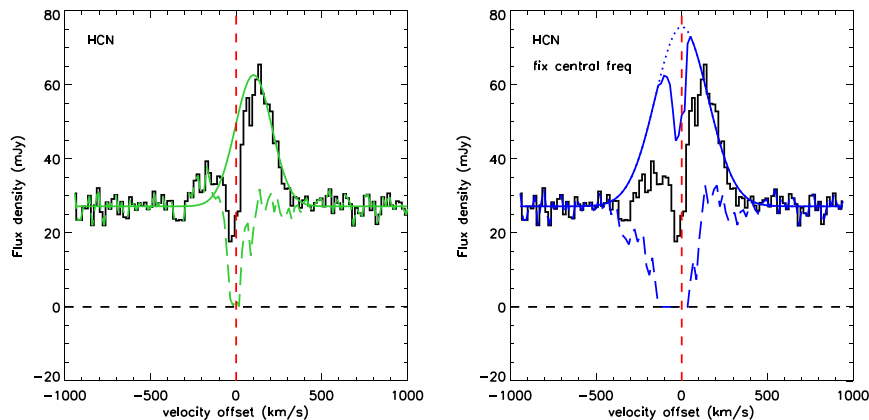
Figure 4. Observed and reconstructed HCN (1–0) line profiles in NGC 3079. In both panels, the observed profile is drawn as a black line, and the reconstructions assume that this is the sum of continuum absorption (occurring over spatial scales of a few milliarcsec associated with radio knot B) and a Gaussian emission line (originating in the disc on scales of several arcsec). Left: the intrinsic profile has been reconstructed with the requirements that the red side of the observed profile is unabsorbed, and that the continuum absorption (dashed green line) cannot go below zero. The resulting intrinsic emission line (solid green line) is redshifted with respect to systemic and also underestimates the weak emission observed on the blue side of the line. In addition, the continuum absorption lacks the blue wing seen in the $H^{13}CN$ profile. Right: the additional requirement that the intrinsic line profile must be centred at the systemic velocity has been applied. The continuum absorption (dashed blue line) is now much broader and extends to velocities of $-400 \, km \, s^{-1}$ consistent with the absorption profile of the $H^{13}CN$ (1–0) line. However, to match the observed line profile, the intrinsic Gaussian emission line (dotted blue line) must be self-absorbed (solid blue line). This is plausible because the disc of NGC 3079 is close to edge-on, so there is considerable gas at large scales in the disc along the line of sight to the nucleus. In addition, the self-absorption is centred roughly at systemic, which would be expected if cool gas within the disc is causing the self-absorption.

$N_H \sim 10^{21} \, cm^{-2}$, if we adopt the same abundance as in Section 5 or as much as a few $\times 10^{22} \, cm^{-2}$ for a more typical lower HCN abundance. The absorption is at the systemic velocity because the disc motion along the line of sight to the nucleus is across the plane of the sky.

Based on our reconstruction, the flux of the self-absorbed HCN (1–0) line is 16.1 Jy km s^{-1} (nearly a factor of 2 greater than the observed flux) while the total flux of the intrinsic Gaussian is 18.7 Jy km s^{-1}. A similar analysis of the HCO$^+$ (1–0) line confirms that it does suffer more from absorption: our estimate of the self-absorbed flux is 13.3 Jy km s^{-1} (nearly a factor of 3 greater than that measured directly) and the intrinsic flux in the Gaussian is 19.5 Jy km s^{-1}. The FWHM of the intrinsic Gaussian profile is 360 km s^{-1}, which we have included in Table 3.

3.1.2 Comparison with single dish measurements

A spectrum of NGC 3079 including the lines discussed above was presented previously by Costagliola et al. (2011). This was based on data from the IRAM 30 m telescope, with a beam size of 29 arcsec at 88 GHz. While the HCN (1–0) and HCO$^+$ (1–0) lines both show a double-peaked profile – which can be generally interpreted as disc rotation or be indicative of either continuum absorption or self-absorption in the centre – their fluxes of 24.6 and 27.7 Jy km s^{-1} are several times greater than observed with our interferometric beam, and the line widths of 500 km s^{-1} FWHM are significantly broader. They also detect a strong blend of C$_2$H emission at about 87 GHz which we detect only weakly. The difference in line fluxes suggests that there is significant, but low-intensity emission from these lines on scales greater than a few arcsec. As is apparent from our data, as one integrates the flux within larger apertures, the absorption below the continuum level is filled in by the additional line emission included in the aperture, and so the line appears broader. It is likely that in the single dish measurement, continuum absorption has only a minor impact, and the double-peaked profile is likely to be due to self-absorption (we note that the dip between the peaks is to

a similar depth as our reconstructed self-absorbed profile). If one does not correct for this, the line width will be overestimated. For the interferometric spectrum in Fig. 4, we can estimate the effective FWHM of the self-absorbed profile by fitting a single Gaussian to the double-peaked profile. Approximating the profile in this way yields an FWHM of 450–470 km s^{-1}, similar to the 500 km s^{-1} width reported by Costagliola et al. (2011) but significantly more than the intrinsic FWHM of 360 km s^{-1}. Similarly, once one corrects for the continuum absorption, the ratio of the HCN (1–0) and HCO$^+$ (1–0) line fluxes is similar to that reported by Costagliola et al. (2011). We conclude that while our spectrum looks rather different from the single dish spectrum, all the differences can be understood as a result of extended low-intensity emission and the aperture-dependent impact of continuum absorption on the observed profile.

3.2 NGC 6764

The 3 mm continuum map is shown in the bottom left panel of Fig. 1. Its FWHM of 1.04 arcsec × 0.82 arcsec and PA of 8° indicate it is spatially unresolved. Within a 3 arcsec aperture, the continuum flux density is 0.6 mJy.

Fig. 1 also shows the integrated HCN (1–0) and HCO$^+$ (1–0) maps in the bottom-middle and right-hand panels, and the measurements and the line fluxes are summarized in Table 3. The HCN (1–0) emission has an extent of 1.7 arcsec × 1.3 arcsec at PA −54°, similar to the 1.7 arcsec × 1.2 arcsec at PA −66° of the HCO$^+$ (1–0) line. The red and blue channels of emission (from line centre to −435 km s^{-1} and +465 km s^{-1} for HCN; to −335 km s^{-1} and +365 km s^{-1} for HCO$^+$) also have the same separation of 0.82 arcsec at PA −87°. Fig. 5 shows integrated spectra covering the two line profiles including a constant continuum level. Their FHWMs are 214 and 203 km s^{-1}, respectively. Taken together, these measurements indicate that the distributions and kinematics of the two lines are very similar, and hence that they originate in the same region. This means that when constructing a simple dynamical model, as discussed in Section 4, we can constrain it using both lines, which
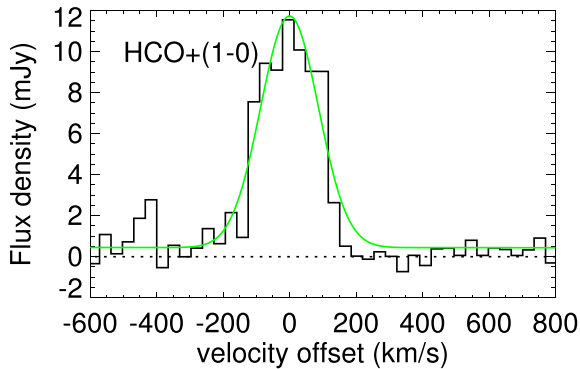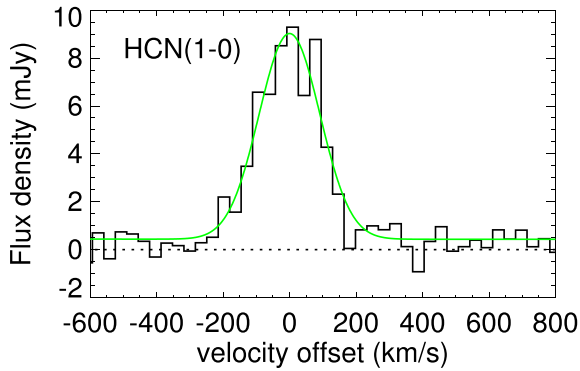
Figure 5. Spatially integrated spectrum for NGC 6764 showing the HCN (1–0) (top panel) and HCO$^+$ (1–0) (bottom panel) emission lines. The continuum has not been subtracted. In each case, the best-fitting Gaussian function is represented by the green line. The line profiles are very similar, showing a large velocity dispersion with a mean FWHM of 209 km s^{-1}.

Figure 6. Spatially integrated spectrum for NGC 5033 showing the HCN (1–0) (top panel) and HCO$^+$ (1–0) (bottom panel) emission lines. The continuum has not been subtracted. In each case the best-fitting Gaussian function is represented by the green line. And the line profiles are very similar, showing a large velocity dispersion with a mean FWHM of 183 km s^{-1}.

provides an additional robustness against limitations of signal to noise or line specific peculiarities.

3.3 NGC 5033

The 3 mm continuum for NGC 5033 is presented in the top left panel of Fig. 1, and has a flux density within a 3 arcsec aperture of 0.7 mJy. A Gaussian fit gives a size of 1.01 arcsec × 0.79 arcsec at PA 41°. As for the other two galaxies, this is consistent with the continuum being spatially unresolved.

The HCN (1–0) and HCO$^+$ (1–0) maps are shown in the top-middle and right-hand panels of Fig. 1, respectively. The measured sizes are 2.0 arcsec × 1.1 arcsec at PA −17° and 1.7 arcsec × 1.2 arcsec at PA 52°, respectively. We note that the latter case, HCO$^+$ (1–0) has a large uncertainty which we attribute to the weaker HCO$^+$ (1–0) line flux. As before, the blue and red contours represent the line emission from blue and red channels (from line centre to −435 km s^{-1} and +465 km s^{-1} for HCN; to −335 km s^{-1} and +365 km s^{-1} for HCO$^+$). Their separations are 1.1 and 1.0 arcsec, respectively. The PA for HCN (1–0) is −17°; the PA for HCO$^+$ (1–0) differs from this but has a large uncertainty because of the low signal to noise in the blue channels, and is still consistent with the HCN (1–0). Fig. 6 shows spectra extracted within a 3 arcsec aperture. The flux of HCN (1–0) is 1.2 Jy km s^{-1} and of HCO$^+$ (1–0) is 0.71 Jy km s^{-1}. The two lines have similar width, with a mean FWHM of 183 km s^{-1}. Again, we find that the distributions and kinematics of the two lines are similar, and hence conclude that they originate from the same region.
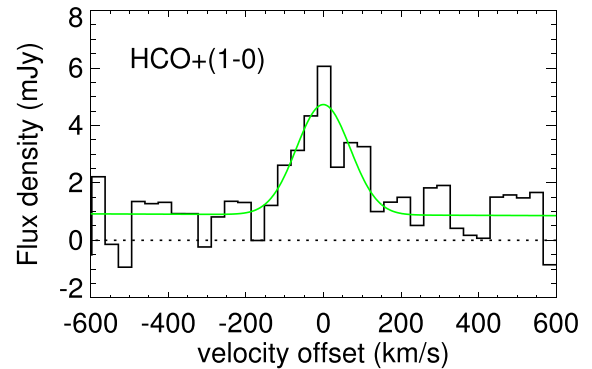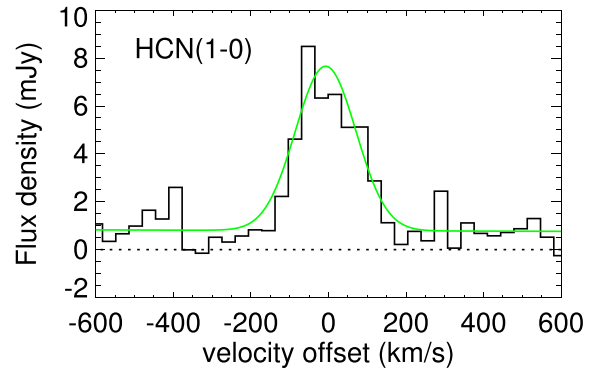
4 MODELLING THE KINEMATICS

The description above of the observed characteristics shows the FWHM of the line is typically 200 km s^{-1}. Comparable line widths for the HCN (1–0) line were reported previously for the central hundred parsecs of several AGN by Sani et al. (2012). Our aim in this section is to understand whether the line widths can be accounted for by a thin rotating disc, or whether it implies there is a significant intrinsic dispersion associated with the molecular disc of dense gas. To do so, we create a simple dynamical model that can match the observed characteristics of the molecular line emission, using the same methodology as Sani et al. (2012).

To constrain our model, we use four of the observed molecular gas properties listed in Table 3: (1) major-axis FWHM, (2) minor-axis FWHM, (3) separation between the centres of the blue and red channel maps, and (4) spectral FWHM of the spatially integrated line. The inclination and PA of the disc are fixed input parameters, as described below. We assume that the line traces a rotating disc and model the observed properties by applying the IDL code DYSMAL (Dynamical Simulation and Modelling Algorithm, described in Davies et al. 2011). The main purpose of this code is to quantify the impact of spectral and spatial beam smearing on an axisymmetric rotating disc. In doing so, it allows us to infer the intrinsic kinematics of the disc from the observed properties. On the other hand, we include NGC 7469 using data presented in Davies et al. (2004). While the HCN (1–0) observations for that object have not been modelled in this way, the 0.7 arcsec resolution 1 mm CO (2–1) and 0.09 arcsec resolution 2.12 μm H$_2$ 1–0 S(1) data enabled those authors to derive a detailed mass distribution based on the

combined dynamics at their different resolutions. This object therefore allows us to directly test whether our simple dynamical model based on a single Gaussian mass distribution can be considered a working approximation in the context of disc size scale, dynamical mass, and ability to distinguish between thin and thick geometries.

4.1 Kinematic modelling procedure

The kinematic modelling procedure we use is the same as described in Sani et al. (2012). However, in addition, we explore the impact of the initial conditions on the convergence of the minimization routine to ensure that we have reached the global rather than local minimum. To do so, we generate a set of random values within broad but restricted ranges for the disc size, disc thickness, and a mass scaling ($M_{\rm scale}$, which is simply a way to set the amplitude of the rotation curve, and represents the mass supported by ordered circular orbits in the disc plane). We then run a minimization starting from these values. At each iteration, it uses DYSMAL to simulate how a disc model with the given properties would appear when convolved with the spatial beam and spectral resolution of our data. The model is based on a Gaussian distribution, the FWHM of which is equal to the given disc size (R is half of this FWHM). The shape and amplitude of the rotation curve is derived from this in combination with the mass scaling $M_{\rm scale}$. Finally, the vertical profile of the disc is defined by a Gaussian distribution, the FWHM of which is equal to the given disc thickness (H is half of this FWHM). The thickness has an observational impact both on the spatial distribution if the disc is inclined, and also on the velocity dispersion which we calculate as $\sigma = vH/R$ and assume is isotropic. The line of sight velocity distribution is derived for each point through the inclined disc model; and, after applying appropriate beam smearing, used to generate an output cube with two spatial axes and one velocity axis. The output data cube is analysed in the same way as the real data, extracting the four properties listed above and comparing them with those extracted from the observations. The minimization routine iteratively converges on a set of disc parameters that lead to a best match of the observed properties. After repeating this process 100 times with different initial parameters, we obtain 100 sets of the best-fitting model output parameters and their corresponding χ^2. We select the 50 sets with the lowest χ^2 and use these to estimate the mean for each model parameter (note that we use the statistical mean rather than the set of parameters from any single minimization), and list

them in Table 4. In a final step, we input the mean values back into DYSMAL one more time and retrieve the simulated output 'observable' properties, which are also listed in Table 4. Together with these output parameters of the model, we list the input parameters (disc size, disc thickness, and scaling $M_{\rm scale}$). To constrain the input parameter uncertainties, we estimate the input parameter distribution (either side of the best-fitting values) that can satisfy the output observable properties within their uncertainties. This is similar in principle to the Markov chain Monte Carlo method, but simplified since we do not require to know the full probability distributions for the input parameters. We list the $\pm 1\sigma$ uncertainties for input parameters in Table 4. We summarize the associated kinematics of the best-fitting rotating disc at a radius R in Table 5, together with the enclosed dynamical mass $M_{\rm dyn}$ which we estimate as $(v^2 + 3\sigma^2)R/G$ (as discussed in Davies et al. 2007 and Sani et al. 2012). Fig. 7 shows the simulated disc models for the three sources with new observations, convolved with the appropriate beam.

4.2 NGC 7469

Although the interferometric beam size at 3 mm is only ∼1 arcsec, this is still relatively large compared to the scale of the nuclear structures. As a result, models are necessarily very simple and we have used a single Gaussian mass distribution to define the rotation curve and emission distribution. Since we are limited to using a very simple model, we use NGC 7469, which has been already successfully modelled with a complex mass distribution, to assess whether our approach is applicable. Davies et al. (2004) constructed a single axisymmetric mass model for NGC 7469 comprising a broad disc, a ring and an extended nucleus to interpret the observations of CO (2–1) and the K-band H$_2$ 1–0 S(1) line at different resolutions. The details of this mass model are summarized in their table 2, and we adopt it for our analysis, calling it the 'complex model'. While the mass distribution represented by these three components is fixed, we represent the HCN (1–0) line emission distribution by a single independent component (i.e. the kinematics of the line are defined by the fixed mass distribution, but the distribution of the line emission does not necessarily follow that of the mass). One additional assumption we make is that all the components share the same thickness. This is a free parameter in the model, as is the size scale of the luminosity distribution, while the mass scale (as before, this represents only the mass supported by ordered circular orbits

Table 4. Summary of simulated disc models: (1) Source name; (2) Molecule; (3) Note; (4) Disc FWHM size in the disc plane; (5) Disc FWHM thickness (height); (6) Scaling $M_{\rm scale}$ (which sets the amplitude of the rotation curve, and represents the mass supported by ordered circular orbits in the disc plane); (7)–(10) are measured with the same method as columns (4), (5), (7), and (9) of Table 3; (11) reduced χ^2 of the fit.

Source	Molecule	Note[a]	Mean value of best-fitting model parameters			four simulated properties from DYSMAL				$\chi^2_{\rm red}$
			Size (arcsec)	Thickness (arcsec)	$\log(M_{\rm scale})$ (M$_\odot$)	Maj. $\times$ min. axis (arcsec^2)	b/r sep. (arcsec)	Line width (km s^{-1})		
NGC 7469	HCN	Complex	$2.41^{+0.01}_{-0.05}$	$0.43^{+0.01}_{-0.03}$	9.95^b	3.15×2.69	1.22	242		6.3
	HCN	Simple	$2.56^{+0.03}_{-0.09}$	$0.62^{+0.03}_{-0.06}$	$9.42^{+0.02}_{-0.02}$	3.27×2.84	1.15	235		4.5
NGC 6764	HCN	–	$1.35^{+0.03}_{-0.10}$	$0.25^{+0.01}_{-0.14}$	$8.66^{+0.05}_{-0.07}$	1.71×1.21	0.74	203		2.2
	HCO$^+$	–	$1.43^{+0.03}_{-0.10}$	$0.26^{+0.01}_{-0.15}$	$8.75^{+0.06}_{-0.04}$	1.77×1.23	0.79	217		6.6
NGC 5033	HCN	–	$1.70^{+0.08}_{-0.15}$	$0.01^{+0.06}_{-0.00}$	$8.47^{+0.05}_{-0.15}$	1.94×1.17	0.98	182		0.7
	HCO$^+$	–	$1.54^{+0.09}_{-0.14}$	$0.19^{+0.08}_{-0.12}$	$8.37^{+0.05}_{-0.15}$	1.85×1.18	0.88	190		0.1
NGC 3079	HCN	–	$2.66^{+0.02}_{-0.03}$	$0.45^{+0.01}_{-0.05}$	$9.30^{+0.03}_{-0.06}$	2.92×1.43	1.51	378		0.9

Notes. The uncertainties given are derived as joint uncertainties and hence implicitly take into account possible partial correlations between parameters.
[a]For NGC 7469 'complex' refers to the multicomponent dynamical model from Davies et al. (2004), 'simple' to the single Gaussian representation for the mass distribution.
[b]Fixed to $M_{\rm scale} = 9 \times 10^9$ M$_\odot$ as given by Davies et al. (2004).

Table 5. Intrinsic kinematics of the modelled rotating discs: (1) Source name; (2) Molecule; (3) Radius (half of the FWHM given in Table 4); (4) Rotational velocity at R; (5) Velocity dispersion at R; (6) Enclosed dynamical mass estimated as $(v^2 + 3\sigma^2)R/G$.

Source	Molecule	R (pc)	v (km s^{-1})	σ (km s^{-1})	$\log(M_{\rm dyn})$ (M$_\odot$)
NGC 7469	HCN[a]	356	131	47	9.30
	HCN[b]	377	128	62	9.39
NGC 6764	HCN	101	102	38	8.54
	HCO$^+$	108	110	40	8.63
NGC 5033	HCN	62	104	1.4	8.20
	HCO$^+$	56	98	25	8.18
NGC 3079	HCN	112	204	69	9.16

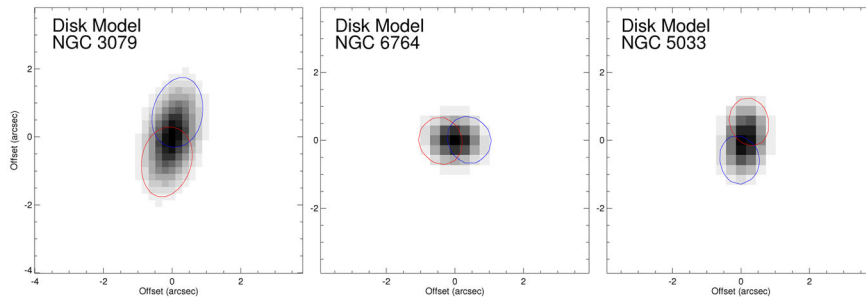*Notes.* [a]Complex model with multiple components; [b]Simple model with 1 component.

Figure 7. Simulated disc models for the three sources with new observations, convolved with the appropriate beam. As for Fig. 1, the grey-scale image shows the emission of the modelled disc while the blue and red contours represent the distribution of integrated blue and red channels of the emission lines (at 50 per cent of the peak intensity). We show the model for only one line, but it is a good representation for both HCN (1–0) and HCO$^+$ (1–0). A PV diagram extracted from the model for NGC 3079 is shown in Fig. 8.

in the disc plane) is fixed to $M_{\rm scale} = 9 \times 10^9$ M$_\odot$ as derived by Davies et al. (2004). When applying our kinematics modelling procedure as described above, the best-fitting values for the disc size and disc thickness are 2.41 and 0.43 arcsec, respectively. And, as summarized in Table 5, accounting for rotation and dispersion, we estimate the dynamical mass to be $\log M_{\rm dyn}[{\rm M}_\odot] = 9.30$. In comparison, when using a single Gaussian profile to define the mass distribution (hereafter called the 'simple model'), we leave the disc size, disc thickness, and mass scale as three free parameters. We then derive best-fitting mean values for disc size and thickness to be 2.56 and 0.62 arcsec, and estimate $\log M_{\rm dyn}[{\rm M}_\odot] = 9.39$. There are two key results here. The first is that the disc size and thickness are consistent between the two models, as is $M_{\rm dyn}$. The second is that the model implies the disc is thick, with an intrinsic $\sigma/v \sim 0.4$. While the dispersion we derive of 50–60 km s^{-1} is larger than the 30 km s^{-1} seen directly in the higher spatial resolution CO (2–1) data by Davies et al. (2004), both would lead to the same conclusion in the context of distinguishing between a thick disc and a thin disc: that a significant intrinsic dispersion is required, and a thin disc is ruled out.

Thus we can estimate the intrinsic kinematics, and in particular the dispersion (thickening), for the disc using a simple approximation to the mass distribution. In the rest of this section, we make use of the simple model to derive the intrinsic kinematics also for NGC 6764 and NGC 5033.

4.3 NGC 6764

When modelling NGC 6764, we assume that the nuclear disc and galactic disc have the same inclination, which we set to 62° (Leon et al. 2007). And we note that the PA of the line emission, as well as

its velocity gradient, are approximately perpendicular to the parsec-scale core-jet structure (PA $\sim$25°; Kharb et al. 2010). We caution that, while the velocity gradient we see at radii up to 1 arcsec is consistent with that of the CO (2–1) line up to radii of 5 arcsec (Leon et al. 2007), our model focusses on the smaller scale and may not represent the properties of the rotating disc at $\gtrsim$200 pc, which might be perturbed by streaming motions associated with the bar.

We perform the kinematics modelling separately on each of the two lines, which independently yield essentially the same solution: a disc with a size of $\sim$1.4 arcsec and a thickness of $\sim$0.25 arcsec. We conclude that the observational constraints require a thick disc model to explain the line emission distribution and kinematics, and in particular the large velocity width of the molecular lines. In our assumption of hydrostatic equilibrium, the disc thickness of the model corresponds to an intrinsic $\sigma/v \sim 0.37$.

4.4 NGC 5033

For NGC 5033, based on the kinematical parameters derived from the CO (1–0) velocity field (Kohno et al. 2003), we fix the inclination to 66°. We note also that the PA on those larger scales matches what we have measured on 1 arcsec scales for the HCN (1–0) and HCO$^+$ (1–0) lines, and is approximately perpendicular to the synchrotron radiation from the core-jet structure, which is oriented east–west (Pérez-Torres & Alberdi 2007).

Our modelling results differ for the two lines. The characteristics of the HCN (1–0) line are well matched by a very thin disc with a size of 1.7 arcsec. In contrast, the HCO$^+$ (1–0) emission is better matched by a thicker disc with a size of 1.54 arcsec and a thickness of 0.19 arcsec. However, due to the low signal to noise of the HCO$^+$ (1–0) line emission, the observable properties have large
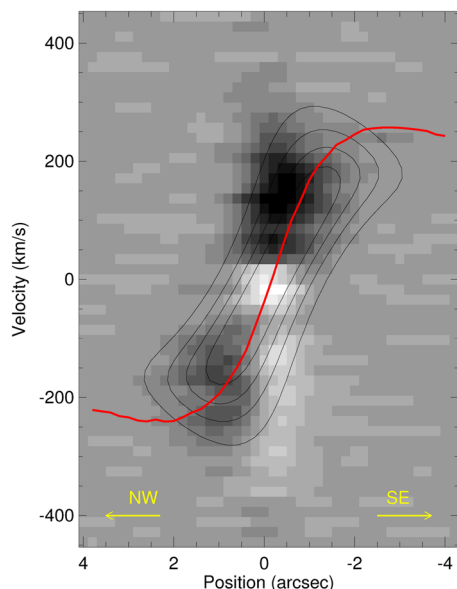
Figure 8. The observed PV diagram (grey scale) for the HCN (1–0) line in NGC 3079, extracted along the major axis (slit 1 arcsec wide at a PA of 165°). The beam-convolved PV diagram from our axisymmetric dynamical model is overplotted as black contours (20 per cent, 40 per cent, 60 per cent, and 80 per cent of the peak intensity). The red line traces the rotation curve derived from it using the iteration method (Takamiya & Sofue 2002). Positive and negative positions indicate the NW and SE directions. respectively.

Table 6. Summary of the kinematic modelling for the combined sample which includes the four Seyferts analysed here and four Seyferts from Sani et al. (2012). (1) Source name; (2) HCN (1–0) Luminosity (3) Radius; (4) Rotational velocity at R; (5) Velocity dispersion at R; (6) Enclosed dynamical mass.

Source	L_{HCN}	R (pc)	v (km s^{-1})	σ (km s^{-1})	M_{dyn} ($M_{\odot}$)
NGC 7469[a]	7.87	356	131	47	9.30
NGC 6764[b]	6.90	101	102	38	8.54
NGC 5033[b]	6.36	62	104	1	8.20
NGC 3079	7.49	112	204	69	9.16
NGC 2273	6.86	97	83	33	8.36
NGC 3227	6.52	23	105	42	7.98
NGC 4051	5.88	22	47	19	7.23
NGC 6951	6.36	45	84	34	8.04

Notes. [a]From the complex model.
[b]We have adopted the model based on the HCN (1–0) line: for NGC 6764, it provides a better fit; for NGC 5033, it provides a better constrained fit.

very well, although, the line emission does shows deviations from axisymmetry (in particular, the south eastern side shows indications for redshifted emission at $V > 200\,\mathrm{km\,s^{-1}}$ at a radial offset of $\lesssim 0.5$ arcsec). We have used the iteration method (Sofue & Rubin 2001; Takamiya & Sofue 2002) to derive the central rotation curve from the beam-convolved model, and overplotted this on the figure. The model compares well with fig. 15 of Koda et al. (2002), where the spatial resolution was slightly poorer than ours, but which was not hampered by absorption.

4.6 Kinematics summary

For three of the four galaxies we have modelled, the nuclear emission line characteristics require a thick disc with $\sigma/v \gtrsim 0.3$. The validity of our results is demonstrated for two objects. For NGC 7469, matching the kinematics of higher resolution CO (2–1) and H$_2$ 1–0 S(1) data to a detailed mass model, Davies et al. (2004) noted that the dispersion of the CO (2–1) line had to be a relatively high $30\,\mathrm{km\,s^{-1}}$. For NGC 3079, focusing on the 'core' component seen in CO (2–1) data, Koda et al. (2002) required a dispersion of $60\,\mathrm{km\,s^{-1}}$ to model the kinematics.

Sani et al. (2012) performed a similar kinematic analysis of the HCN (1–0) line for four other nearby Seyfert galaxies, finding σ/v in the range 0.3–0.5 for all of them. We combine these with our kinematic analysis above and summarize the combined modelling results in Table 6. We find that in seven out of eight nearby Seyferts, $\sigma/v \gtrsim 0.3$. Only for NGC 5033, do we find evidence that the disc is thin, with $\sigma/v \lesssim 0.1$. We conclude that thick molecular disc are a common occurrence in the central ~ 100 pc of Seyfert galaxies.

5 COLUMN DENSITY THROUGH THE INNER DISC OF NGC 3079

In this section, we use the depth of the absorption features in the spectrum of NGC 3079 to make a direct estimate of the gas column density of the disc, and discuss the origin of the absorption features.

We already noted in Section 3.1 that the H^{12}CN (1–0) absorption is saturated, making it difficult to use reliably to derive column density. Instead, the H^{13}CN (1–0) is an ideal transition for this purpose, not only because it is unsaturated but also because its frequency is far enough away from other transitions that it is unblended. The

uncertainties and so the model is poorly constrained, as reflected in the very small χ^2 for this fit. For this object there is no convincing evidence for a thick disc. We conclude that our kinematic analysis favours the thin disc solution, for which the corresponding intrinsic σ/v ratio is <0.1.

4.5 NGC 3079

Despite the absorption in the molecular emission lines, we still apply the kinematics modelling to HCN (1–0); however, we exclude HCO$^+$ (1–0) since the effect of the absorption is too severe. According to the kinematical parameters derived from the CO (1–0) velocity field (Koda et al. 2002), we fix the nuclear disc inclination to 77° and PA to 165°. In addition, to reduce any bias caused by the impact of the absorption in setting the amplitude of the rotation curve, we also fix $M_{scale} = 2 \times 10^9\,M_{\odot}$ (at 3 arcsec) based on the value derived by these authors from their kinematical modelling of the CO (2–1) line of their 'core' component, which we identify as the component traced by the HCN (1–0) and HCO$^+$ (1–0) lines. The best-fitting mean values for the disc size and thickness are 2.66 and 0.45 arcsec. The associated dispersion is just under $70\,\mathrm{km\,s^{-1}}$, consistent with the $60\,\mathrm{km\,s^{-1}}$ of Koda et al. (2002), and confirms that the dense clouds exhibit significant intrinsic random motions. The observed line emission distributions and kinematics need the thick disc geometrical structure, the corresponding intrinsic σ/v ratio is ~ 0.33.

Since the emission lines are better spatially resolved in NGC 3079 than the other targets, we plot a position-velocity (PV) diagram in Fig. 8 extracted along the major axis. The grey-scale image shows that emission as darker colours and the absorption in lighter colours. Superimposed are contours tracing our axisymmetric dynamical model. Given the simplicity of this model, it traces the emission

spectral profile of the absorption from this line is shown in panel (c) of Fig. 3, and the systemic velocity, for which we have adopted $1147 \, \text{km s}^{-1}$ (Koda et al. 2002), is drawn as a dashed red line. The solid blue line represents the continuum flux density within the 3 arcsec aperture. The deeper absorption (the component close to the systemic velocity) is denoted 'C1'; the broader absorption component (furthermore blueshifted from the systemic velocity) is denoted as 'C2'.

5.1 Column densities

Assuming that local thermal equilibrium conditions hold, the velocity-integrated optical depth can be used to derive the total column density of molecules (Wiklind & Combes 1995). For an absorption line J $\rightarrow$ J + 1:

$$N_{\text{total}} = \frac{8\pi}{c^3} \frac{\nu^3}{A_{J+1,J} g_{J+1}} \frac{Q(T_{\text{ex}})\exp(E_J/kT_{\text{ex}})}{1 - \exp(-h\nu/kT_{\text{ex}})} \int \tau_\nu \, dV, \quad (1)$$

where $A_{J+1,J}$ is the Einstein A coefficient, $g_{J+1} = 2J + 1$ is the statistical weighting of level J, E_J is the energy of level J, $Q(T_{\text{ex}}) = \sum_{J=0}^{\infty} g_J \exp(-E_J/kT_{\text{ex}})$ is the partition function, and $\int \tau_\nu dV$ is the velocity-integrated optical depth. In order to calculate this, we have used coefficients from the Leiden Atomic and Molecular Database (Schöier et al. 2005), for which the energy levels and radiation transitions extend up to $J = 29$. The excitation temperature, T_{ex}, is set as 4 K which is consistent with a high opacity of the lower transitions and, as concluded for NGC 5128 by Muller & Dinh-V-Trung (2009), is expected for densities up to $\sim 10^4$ cm^{-3}. We estimate the optical depth over the source as

$$\tau_\nu = -\ln\left(\frac{I_\nu^{\text{obs}}}{I_\nu^{\text{cont}}}\right), \quad (2)$$

where I_ν^{obs} is the observed flux density of the absorption feature and I_ν^{cont} is the continuum flux density transmitted by the background non-thermal radio sources.

The velocity integrated optical depths of C1 and C2 are 46.13 and $80.88 \, \text{km s}^{-1}$, from which we estimate associated column densities for H^{13}CN of 1.5×10^{14} and 2.6×10^{14} cm^{-2}, respectively. In order to derive the hydrogen column density N_{H}, we need to apply two corrections. The first one is for the ^{12}C/^{13}C isotope ratio, which we assume to be 60, similar to the local interstellar medium (Milam et al. 2005). However, we note that this conversion may be underestimated if the circum-nuclear region has a high star formation rate, for example, M 82 and NGC 253 have ^{12}C/^{13}C ~ 100 (Martín et al. 2010). The second correction is for the H^{12}CN abundance X_{HCN}. (Harada, Herbst & Wakelam 2010) have calculated values in the range 3×10^{-6}–9×10^{-9} for gas on scales of a few to tens of parsecs around an AGN, depending on time-scale. These values are for warm (~ 100–400 K) gas, similar to the molecular gas temperatures found in the central regions of Seyfert galaxies (Krips et al. 2008; Davies, Mark & Sternberg 2012; Hailey-Dunsheath et al. 2012; Viti et al. 2014). In the absence of specific constraints, we adopt the geometrical mean of these two values, $X_{\text{HCN}} \sim 10^{-6.8}$, which is consistent with the plentiful evidence for X-ray-enhanced HCN abundance around AGN. Consequently, N_{H} for the C1 and C2 components is $\sim 5.6 \times 10^{22}$ and $\sim 9.8 \times 10^{22}$ cm^{-2}, respectively.

Support for the high column density in the central disc of NGC 3079 comes from the SiO absorption. Numerous observations have shown that SiO is commonly found in massive star-forming regions and in shocked clumps related to supernova remnants (e.g. Downes et al. 1982; Ziurys, Snell & Dickman 1989a). And enhancement of the SiO abundance has been predicted in high-temperature

chemistry reactions and models which contain shocks or molecular formation in fast molecular outflows (Martin-Pintado, Bachiller & Fuente 1992; Klaassen & Wilson 2007).

We estimate SiO column densities for components C1 and C2 in NGC 3079 as $\sim 2.8 \times 10^{14}$ and $\sim 3.4 \times 10^{14}$ cm^{-2}, respectively. For both components the ratio of SiO abundance to HCN is in the range 0.02–0.03. These ratios are significantly higher than found in dark clouds or quiescent regions (where ratios $\lesssim 0.003$ are expected), but also significantly less than the range 0.1–1 found in massive star-forming regions. They are more comparable to the perturbed clouds associated with supernova remnant IC 443 where $X_{\text{SiO}}/X_{\text{HCN}} \sim 0.04$–$0.06$ (Ziurys, Friberg & Irvine 1989b), and also to the circum-nuclear disc of NGC 1068 where $X_{\text{SiO}}/X_{\text{HCN}} \sim 0.06$–$0.1$ (Usero et al. 2004). Adopting $X_{\text{SiO}} \sim 0.5$–1×10^{-8} as found by Usero et al. (2004) for NGC 1068, we estimate column densities of 0.3–1×10^{23} cm^{-2} for C1 and C2 in NGC 3079.

We note that comparison with N_{H} derived from X-ray spectra towards the AGN is difficult. An estimate based on a *BeppoSAX* observation was $N_{\text{H}} \sim 10^{25}$ cm^{-2} (Iyomoto et al. 2001), while another based on *Chandra* observations was $N_{\text{H}} \sim 2 \times 10^{22}$ cm^{-2} (Cecil, Bland-Hawthorn & Veilleux 2002). On the other hand, both X-ray observatories did strongly detect the Fe K α complex at 6.4 keV, which is a fluorescence line produced when nuclear continuum radiation is reprocessed by circum-nuclear material, and is consistent with heavy absorption.

5.2 Origin of the absorption

The central velocities of C1 and C2 are 29 and $137 \, \text{km s}^{-1}$, respectively. This double-peaked absorption not only appears in several molecules (e.g. H^{13}CN, H^{13}CO^{+}, SiO and HN^{13}C) in the spectrum in Fig. 3, but is also present in the OH absorption observed on milli-arcsec scales with the European VLBI Network (Hagiwara, Klöckner & Baan 2004). Although different observations use distinct molecules, the velocity difference between the two absorption features has a consistent value of $\sim 100 \, \text{km s}^{-1}$.

5.2.1 Component C1

Owing to the alignment of the water maser distribution with the kiloparsec-scale CO molecular structure, Trotter et al. (1998) proposed a highly inclined molecular disc, oriented roughly north–south, as the geometry of the nuclear region in NGC 3079. In addition, Kondratko et al. (2005) measured the water maser kinematics and concluded the presence of a relatively thick and flared disc structure in the centre. We adopt these ideas from the literature and suggest that the deeper absorption C1 originates from the blueshifted part of the rotating molecular disc, which lies in front of the bright radio jet continuum source B, which we discussed in Section 3.1 as also being one of the primary sources of the 3 mm continuum. Adopting a black hole mass 2×10^6 M$_\odot$ (Kondratko et al. 2005), and taking into account the inclination of the rotating disc and the location at which the absorption is occurring, we estimate that the velocity associated with the disc absorption should be $-47 \, \text{km s}^{-1}$, in good agreement with the observed velocity of component C1. In contrast, the redshifted part of the rotating molecular disc is located behind the other prominent radio jet continuum source, A; and therefore no equivalent redshifted absorption occurs in the spectrum. This scenario of off-centre absorption in the nuclear region of NGC 3079 is illustrated in the right-hand panel of Fig. 9. Based on this scheme, we argue that C1 may trace the intrinsic
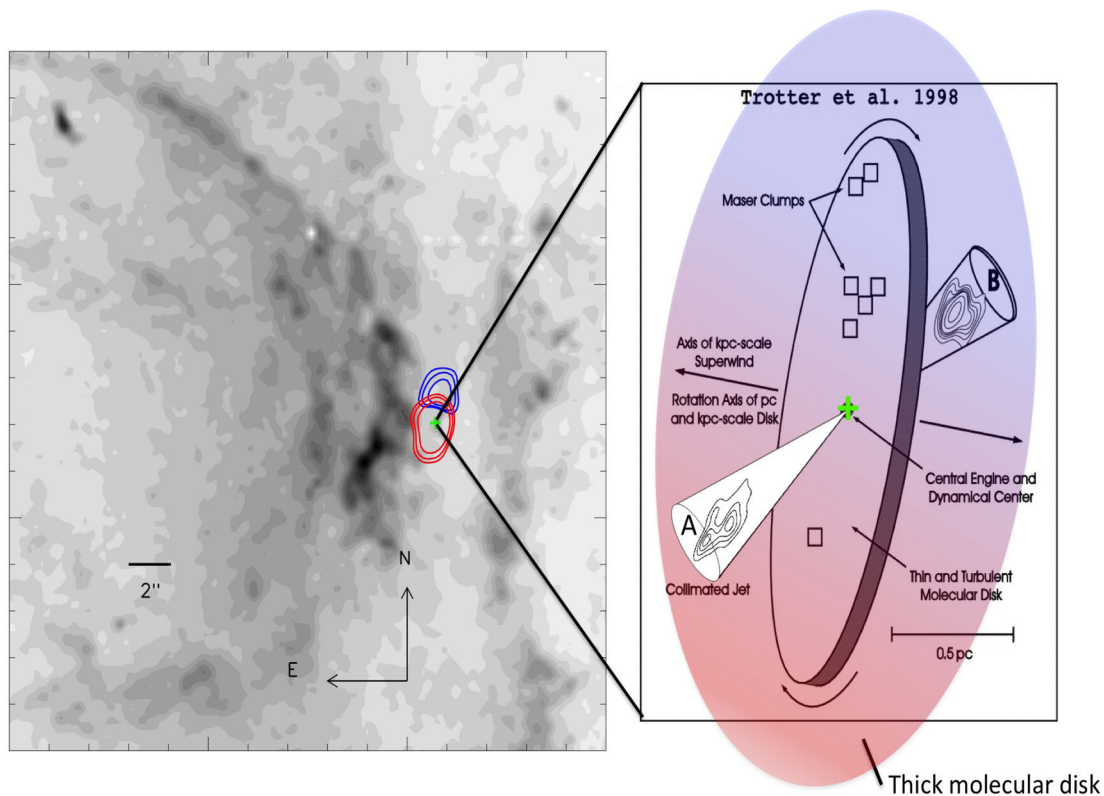
Figure 9. Left-hand panel: grey-scale image is the [N II] + Hα map of the superbubble and ionized filaments observed by *HST* (Cecil et al. 2001). The blue and red contours are the distribution of integrated blue and red channels of $H^{12}CN$ (1–0) presented in this paper. The central green symbol indicates the position of the nucleus. Right-hand panel: the distribution of maser emitters (open squares) and 22 GHz radio continuum (grey contours) in the nuclear region of NGC 3079, adapted from Trotter et al. (1998) and Kondratko et al. (2005). The pale blue–red colour gradient across the ellipse represents the kinematics we have observed for the rotating molecular disc. The bright radio component B in the collimated jet to the NW lies behind the disc and causes the blueshifted absorption in the 3 mm continuum. The cone to the SW represents the collimated jet and radio component that lies in front of the disc, and so has been left uncoloured. The green plus symbol marks the dynamical centre adopted by Kondratko et al. (2005) in their maser kinematics model.

column density of neutral hydrogen in the edge-on rotating molecular disc, which we conclude is therefore $N_H \sim 6 \times 10^{22}$ cm^{-2}.

Despite the size of our 3 mm beam, this column is measured at radial scales of ∼1 pc because that is the projected location of the continuum against which the absorption is occurring. If it applies throughout the nuclear disc, we can estimate a gas mass that we can compare with the dynamical mass M_{dyn} from Section 4, and hence estimate a gas fraction. Assuming that the absorption is caused by only 1–2 clouds along the line of sight, so that no inclination correction is required, the gas mass within a radius of 112 pc (the same as that used to derive M_{dyn}) is 2×10^7 M$_\odot$. For $\log M_{dyn}[M_\odot] = 9.16$ (Table 5), we find a gas fraction $f_{gas} = 1.3$ per cent.

These numbers are remarkably similar to the estimates of Hicks et al. (2009). Based on direct CO measurements as well as typical gas fractions for local spirals and star formation galaxies, these authors who argued that even with a low gas fraction of 1 per cent the columns exceed 10^{22} cm^{-2} on scales out to several tens of parsecs, and values are more typically a few 10^{23} cm^{-2}. Their estimates based on extinction to the stellar continuum (assuming the obscuring material is mixed with the stars) suggested slightly lower values with a mean of 2.4×10^{22} cm^{-2}. Our independent measurement based on absorption confirms that in NGC 3079, although the gas fraction in the nucleus is low, there is still sufficient material on scales of at least several parsecs to cause significant optical obscuration from some directions.

5.2.2 Component C2

Absorption component C2 has a broad wing that extends to at least 200 km s^{-1} blueward from the central velocity of C2. Component C2 could be associated with OH absorption (Hagiwara et al. 2004). But in contrast to the extended HCN velocity profile, the OH absorption observed with 45-mas resolution (∼4 pc) shows only the deep absorption of C2 without the broad blueshifted wing. We suggest below that the broad wing could be caused by absorption in outflowing material. The Hα features resembling outflow in the nuclear region of NGC 3079 are displayed in the left-hand panel of Fig. 9. The brightest emission shows that the bubble apex is close to the nucleus, and shocks induced in the bubble wall extend out to large scales tracing the extent of the super wind (Veilleux et al. 1994). An ionized filament with a blueshifted velocity of 125 km s^{-1} relative to systemic lies at a distance of ∼400 pc (4–5 arcsec) from the nucleus, and its morphology aligns with the very long baseline interferometry (VLBI)-scale radio jet (Cecil et al. 2001). We speculate that the broad blueshifted wing – and hence the whole of component C2 – may trace outflows on projected scales larger than 4 pc but smaller than ∼40 pc (noting that this corresponds to half the 1 arcsec FWHM of the IRAM beam). This would imply a column density in the outflowing material of $N_H \sim 10^{23}$ cm^{-2}, comparable with that of the material in the disc. While this seems remarkably high, outflowing material with a similar high $N_H \sim 5 \times 10^{22}$ cm^{-2}
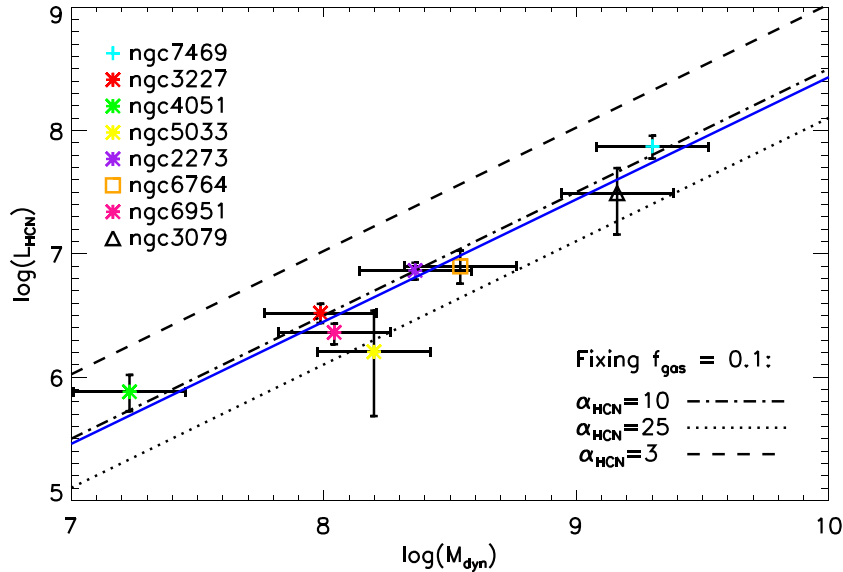
Figure 10. HCN luminosity plotted against dynamical mass for AGN analysed here and in Sani et al. (2012). The uncertainty in HCN luminosity includes errors from HCN flux density and distance. We adopt an uncertainty in dynamical mass of 40 per cent (see the text in Section 6 for details). The solid blue line is the best-fitting linear relation for this data set. According to equation (7), and assuming a gas fraction of 10 per cent, the three black lines represent different HCN conversion factors: $\alpha_{HCN} = 3$ (dashed), $\alpha_{HCN} = 10$ (dot–dashed), and $\alpha_{HCN} = 25$ (dotted).

has been reported for the Seyfert 2 galaxy NGC 1433 (Combes et al. 2013).

6 HCN LUMINOSITY AND DYNAMICAL MASS

In this section we explore the relation between HCN luminosity L_{HCN} and dynamical mass M_{dyn} in the central $\sim$100 pc of Seyfert galaxies, and its implications. We use the combined sample of eight Seyferts with 1 arcsec HCN (1–0) observations and kinematical modelling, as given in Table 6.

Following Gao et al. (2007), the HCN luminosity is calculated as

$$L_{HCN} = 4.1 \times 10^3 \, S_{HCN} \Delta v \, (1 + z)^{-1} \, D_L^2 \qquad (3)$$

in units of K km s^{-1} pc^2, where $S_{HCN}\Delta v$ (Jy km s^{-1}) is the velocity-integrated HCN flux density and D_L (Mpc) is the luminosity distance. Since all our objects are in the very local Universe, the $(1 + z)^{-1}$ term is approximately unity. The uncertainty in HCN luminosity includes uncertainties from the velocity integrated flux density as well as the distance.

The uncertainties on M_{dyn} are difficult to quantify robustly because of the assumptions and simplifications in the kinematic model from which M_{dyn} is derived. For the galaxies they modelled, Sani et al. (2012) state that the random errors are 15–20 per cent excluding the uncertainty for the σ term. From our modelling, which provides a more statistical estimate of the uncertainties based on the distribution of parameters in the best-fitting models, the uncertainties are 30–40 per cent. However, we (and also Sani et al. 2012) adopted fixed inclinations and did not take their uncertainties into account. The inclinations we have used for each galaxy are given in the relevant subsections of Section 4, and we note that in all of the objects we have modelled as well as all of those modelled by Sani et al. (2012) the PA of the nuclear HCN emission matches rather well the PA of the host galaxy on larger scales. Since a warp is likely to alter the PA (as well as the inclination), the similarity of the PA on large and small scales suggests the impact of any warp on the

observed orientation should be modest. We therefore have simply adopted the same inclinations as measured on large scales, noting that for NGC 7469, Davies et al. (2004) report that a 5° change in inclination changes the dynamical mass by 17 per cent. An effect of this size does not increase our uncertainties significantly, and so we adopt a global uncertainty of 40 per cent on all the dynamical mass estimates.

We have plotted L_{HCN} against M_{dyn} in Fig. 10, which shows that the relation between them is essentially linear. The bivariate regression fit (solid blue line on the figure) is given as

$$\log L_{HCN} = (0.99 \pm 0.1) \log M_{dyn} - (1.48 \pm 0.84). \qquad (4)$$

We find that Spearman's rank correlation coefficient $\rho \sim 0.90$ with 98 per cent significance (noting that $\rho = 1$ corresponds to two variables being monotonically related). Since we do not know the intrinsic L_{HCN} for NGC 3079, we adopt the $S_{HCN}\Delta v$ from the absorption corrected flat-topped profile. Its L_{HCN} large uncertainty is due to the difference in flux between the observed line and the absorption-corrected profile. We also looked at the surface densities for the mass and luminosity, where both axes in Fig. 10 are divided by the best-fitting model disc area. A significant correlation still exists, indicating that disc size may not influence the relation between L_{HCN} and M_{dyn}. We discuss below the implication of the mass–luminosity relation in terms of the gas fraction f_{gas} and the conversion factor α_{HCN} between HCN luminosity and gas mass.

For either a single virialized (gravitationally bound) cloud, or a non-overlapping ensemble of such clouds, the ratio α_{HCN} between the gas mass M_{gas} and the HCN luminosity L_{HCN} (in units of K km s^{-1} pc^2) can be written as (Solomon, Radford & Downes 1990; Downes, Solomon & Radford 1993; Krips et al. 2008):

$$\frac{M_{gas}}{L_{HCN}} \equiv \alpha_{HCN} = 2.1 \, n_{H2}^{0.5} \, T_b^{-1} \qquad (5)$$

where n_{H2} (cm^{-3}) is the average H$_2$ number density and T_b (K) is the brightness temperature.

However, as discussed by Downes et al. (1993) and Solomon & Vanden Bout (2005), when the line width traces the potential of a

galaxy, i.e. $\Delta v^2 = G M_{\mathrm{dyn}}/R$, one has to modify equation (5) to account for the mass contributed by stars in addition to the gas. As we have shown in Section 4, this is the case for our observations of the HCN (1–0) lines; and in Section 7, we show that in at least one galaxy the clouds are not self-gravitating. In addition, we also note that since the HCN (1–0) transition has a critical density of $\sim 3 \times 10^6$ cm^{-3} (e.g. Meijerink et al. 2007), the emission traces preferentially dense gas, whereas there may also be a significant mass of gas in less dense clumps, which might instead be traced by CO (1–0) which has a much lower critical density. Following the argument given in Downes et al. (1993), the relation between dynamical mass and HCN luminosity can be expressed as:

$$\frac{M_{\mathrm{dyn}}}{L_{\mathrm{HCN}}} = 2.1 \, n_{\mathrm{eq}}^{0.5} \, T_{\mathrm{b}}^{-1}, \qquad (6)$$

where n_{eq} is an equivalent H$_2$ number density. Then, since $f_{\mathrm{gas}} \equiv M_{\mathrm{gas}}/M_{\mathrm{dyn}} = n_{\mathrm{H2}}/n_{\mathrm{eq}}$, equation (6) can be rewritten as

$$\frac{M_{\mathrm{dyn}}}{L_{\mathrm{HCN}}} = f_{\mathrm{gas}}^{-1/2} \, \alpha_{\mathrm{HCN}} \qquad (7)$$

That there is a relation between L_{HCN} and M_{dyn} which is close to linear, as is apparent in Fig. 10, implies either that there is an intrinsic relation between f_{gas} and α_{HCN} or that there are typical values (to within a factor of 2 or so) for both of these quantities.

Based on a variety of sources and methods, Hicks et al. (2009) argued that the typical gas mass fraction lies in the range 4–25 per cent, with a typical value of $f_{\mathrm{gas}} \sim 0.1$, within the central 200 pc of Seyferts. We adopt this value and, based on equation (7), draw in Fig. 10 the lines corresponding to $\alpha_{\mathrm{HCN}} = 3$ (long dashed line), 10 (dot–dashed line), and 25 (dotted line). We find that $\alpha_{\mathrm{HCN}} = 10$ M$_\odot$ (K km s^{-1} pc^2)$^{-1}$ provides a remarkably good approximation to the data. A similar HCN conversion factor $\alpha_{\mathrm{HCN}} = 10^{+10}_{-3}$ for nearby AGN (albeit with beam sizes ranging from a few arcsec up to 20 arcsec) was found via LVG analysis by Krips et al. (2008). As they noted, it is ~ 2 times smaller than the $\alpha_{\mathrm{HCN}} = 25$ estimated by Gao & Solomon (2004) for nearby spiral, infrared-luminous, and ultraluminous galaxies. However, Fig. 10 rules out such a high conversion factor for the centres of AGN since it would imply a gas fraction exceeding 50 per cent. The difference may point towards differing excitation conditions and molecular abundances in the environments, and there is plentiful theoretical and observational evidence that X-ray excitation of gas by the AGN does have a major impact on both of these leading to an increase in the HCN luminosity (Lepp & Dalgarno 1996; Maloney et al. 1996; Kohno et al. 2003; Usero et al. 2004; Boger & Sternberg 2005; Meijerink & Spaans 2005; Krips et al. 2007; Meijerink et al. 2007; Krips et al. 2008; Davies et al. 2012).

7 NON SELF-GRAVITATING CLOUDS IN NGC 6951

In their high spatial resolution analyses of the Br γ hydrogen recombination line in Seyferts, Davies et al. (2007) and Hicks et al. (2013) were able to show that there was no ongoing star formation in the central ~ 100 pc. And as part of their analysis of the HCN line kinematics, Sani et al. (2012) found that while there was often star formation occurring in circum-nuclear rings at radii $\gtrsim 100$ pc, on smaller scales the evidence indicates that the star formation rates were much lower. Our aim in this section is to assess whether the clouds in the central region are self-gravitating. If they are not, this could be one reason why star formation appears to be suppressed on these scales.

We focus on NGC 6951 which is one of the Seyfert galaxies in the combined sample summarized in Table 6, and for which suitable data are available. Observations reported by Krips et al. (2007) provide the HCN (1–0)/CO (2–1) ratio, which is 2.5 (if units for line fluxes are K km s^{-1}, it is 0.37 if the line flux units are Jy km s^{-1}) as discussed by Davies et al. (2012). These data have similar small beams and so are spatially resolved, which is important since the distributions of the two lines are very different. Here we use the line ratio corresponding to the central component only. In addition, Krips et al. (2008) reported the HCN (3–2)/HCN (1–0) line ratio as 0.4 corrected for beam filling factors. Although the beam for these data is larger [and specifically, the HCN (1–0) measurement used for this line ratio is a single dish measurement rather than the interferometric measurement used for the other line ratio], it is less critical since both lines are from HCN and so are expected to have more similar distributions. Since the beam includes the circum-nuclear ring, there is some uncertainty associated with whether the line ratio reflects that in the nucleus. However, a similar measurement by Krips et al. (2008) on NGC 1068 with a smaller beam that probes only regions well within the circum-nuclear ring, yielded a HCN (3–2)/HCN (1–0) ratio of 0.21 [as such, given the HCN (1–0)/CO (2–1) ratio from Usero et al. (2004) discussed by Davies et al. 2012, the analysis below could equally apply to NGC 1068]; and a ratio of 0.15 has been reported for the nucleus of NGC 1097 by Hsieh et al. (2012). While these two galaxies could also be used for this analysis, we have not included them here. This is partly because they are not part of our combined sample. For NGC 1068, it is also because the nuclear region of NGC 1068 is very complex, having a circum-nuclear bar feeding gas in to the nucleus while an outflow from the AGN disrupts the disc (Müller-Sánchez et al. 2009; Krips et al. 2011; Garciá-Burillo et al. 2014). For NGC 1097, it is also because the AGN is very weak and cannot really be classified as a Seyfert. As can be seen in Fig. 11 even a large uncertainty in the HCN (3–2)/HCN (1–0) ratio does not alter the general conclusion that the clouds cannot be self-gravitating.

In order to derive the physical conditions under which these line ratios can arise, we make use of the LVG approximation (Sobolev 1957), which has been widely used in the literature to study gas conditions and excitation in normal and active galaxies. It is important to realize that LVG calculations apply to individual clouds. On the other hand, the observations we use are of an ensemble of clouds. However, under the usual assumption that all the clouds in the ensemble are the same, the line ratios will not depend on the number of clouds: they will be the same for a single cloud and for the ensemble. We note, however, that this is not the case for the line width, which is very different for a single cloud and for the ensemble. As such, to interpret the modelled ratio $N_{\mathrm{H_2}}/\mathrm{d}V$, or equivalently $n_{\mathrm{H_2}}/(\mathrm{d}V/\mathrm{d}r)$, in the context of the observations would require additional assumptions that one sees all the clouds and that their individual line profiles and relative velocities combine to match the observed line profile. However, our results are not affected by this issue because our comparison of the LVG calculations to observations is based solely on line ratios.

We use the LVG calculations performed by Davies et al. (2012) (we refer to that paper for details of the code and comparison to the commonly used RADEX) and extended them to include the HCN (3–2)/HCN (1–0) line ratio. The calculations cover a wide range of parameters: kinetic temperature $30 \leq T\,[\mathrm{K}] \leq 300$, HCN to CO abundance ratio $10^{-5} \leq X_{\mathrm{HCN}}/X_{\mathrm{CO}} \leq 10^{-2}$ (with $X_{\mathrm{CO}} = 10^{-4}$ as the CO abundance relative to hydrogen), H$_2$ volume gas density $10^3 \leq n_{\mathrm{H_2}}\,[\mathrm{cm}^{-3}] \leq 10^7$, and a ratio of gas-density to velocity-gradient, or equivalently column density to line width, of
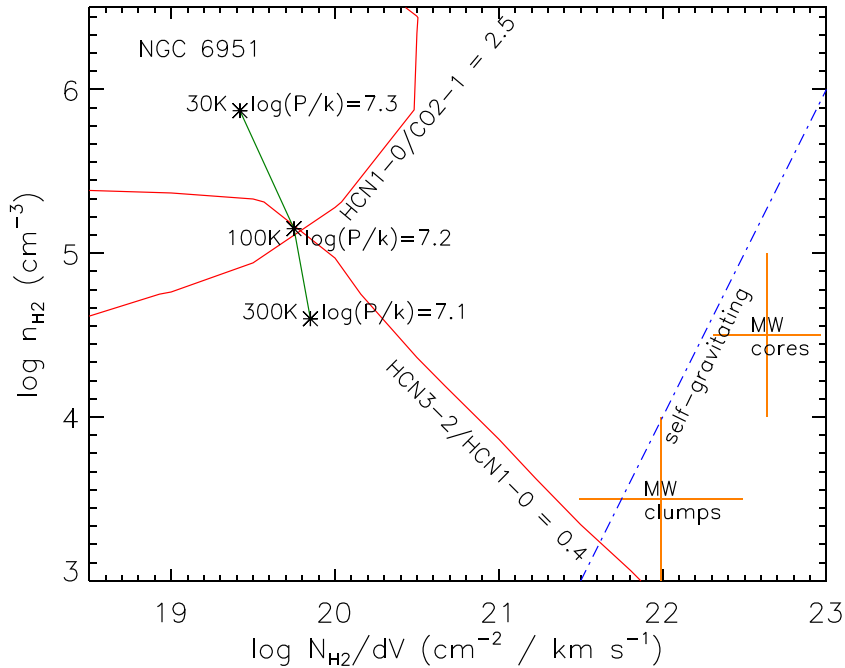
Figure 11. Part of the four-dimensional parameter space for LVG calculations. In this plane, the dot–dashed blue line indicates the boundary for self-gravitating clouds; clumps and cores of Milky Way clouds are located to the right of this (Bergin & Tafalla 2007). Red lines tracing the HCN (1–0)/CO (2–1) and HCN (3–2)/HCN(1–0) ratios in the centre of NGC 6951 have been drawn for $\log X_{\rm HCN}/X_{\rm CO} = -2$ and a temperature of 100 K (see Davies et al. 2012). These lines intersect at a point where the implied pressure in the cloud is $\log P/k\,[{\rm cm}^{-3}{\rm K}] = 7.2$. Due to the well-known degeneracy between density and temperature, these two parameters cannot be fully constrained. But the intersection of lines tracing the two ratios are also shown for temperatures in the range 30–300 K (asterisks joined by solid green lines), and show that the cloud density is likely to be $\log n\,[{\rm cm}^{-3}] = 4.5$–6 and that over this range the pressure in the clouds remains high and roughly constant. Since all the intersections (marked by asterisks) are far to the left of the locus for self-gravitating clouds, the clouds in NGC 6951 must be pressure confined rather than self-gravitating.

$5 \times 10^{17} \le N_{\rm H_2}/{\rm d}V\,[{\rm cm}^{-2}\,({\rm km\,s}^{-1})^{-1}] \le 5 \times 10^{23}$. One plane of this parameter space is shown in Fig. 11.

For reference, we show the boundary (dot–dashed blue line), to the right of which clouds are self-gravitating (see Goldsmith 2001; Davies et al. 2012). For virialized clouds $\Delta V/R \sim n^{0.5}$, where ΔV is the velocity dispersion, R is the cloud radius, and n is the gas volume density. The self-gravitating boundary line is found by treating $\Delta V/R$ as a velocity gradient, which gives ${\rm d}V/{\rm d}r \propto n_{\rm H_2}^{0.5}$ as shown.

We have also marked the regions where one expects to find Galactic clumps and cores, using the typical properties summarized by Bergin & Tafalla (2007) and estimating $N_{\rm H_2}/{\rm d}V$ from their density, size, and velocity width. Galactic clouds, with densities of $n_{\rm H_2} = 50$–500 cm^{-3}, are outside the range of the plot. Their sizes of 2–15 pc and velocity widths of 2–5 km s^{-1} indicate they have $\log N_{\rm H_2}/{\rm d}V \sim 20.9$ and so lie just left of the extension of the self-gravitating line.

We now discuss how, although the LVG calculation formally has five free parameters, we can reach a robust conclusion with only two line ratios. The first parameter is the CO abundance $X_{\rm CO}$, but because this hardly varies for a wide variety of conditions we fix it at $X_{\rm CO} = 10^{-4}$. The HCN abundance $X_{\rm HCN}$ is also a parameter. But it was already shown by Davies et al. (2012) that the HCN (1–0)/CO (2–1) ratio alone requires an unusually high HCN abundance, $X_{\rm HCN} \gtrsim 10^{-6}$. Since this is already much higher than the typical abundance, although still consistent with what one might expect theoretically from calculations of equilibrium abundances in X-ray-irradiated gas (Boger & Sternberg 2005), we fix it at $X_{\rm HCN} = 10^{-6}$.

The volume density $n_{\rm H_2}$ and ratio of column density to line width $N_{\rm H_2}/{\rm d}V$ are the axes of the plot and therefore left as free parameters. Finally, the temperature T is unconstrained. We have therefore plotted red curves tracing the locus of the line ratios above for NGC 6951 assuming a temperature of 100 K; and show in addition the location where the two curves intersect for temperatures of 30 K and 300 K (asterisks joined by the green curve), a range that covers the temperatures one might expect to find in the central regions of Seyferts (Krips et al. 2008). This shows the well-known degeneracy between temperature and density, but also indicates that, unless the temperature of the molecular gas significantly exceeds 300 K, the gas density must be $\log n_{\rm H_2}\,[{\rm cm}^{-3}] \gtrsim 4.5$.

One very clear conclusion from the figure is that, independent of temperature and density, the locus of intersections for the line ratios lies far to the left of the region where one finds self-gravitating clouds. Indeed, for the range of temperatures we have considered, the inferred pressure is roughly constant at $P/k = (1 - 2) \times 10^7\,{\rm cm}^{-3}$ K suggesting that the clouds are likely to be pressure confined. A similar conclusion was reached by Zaragoza-Cardiel et al. (2014) for H II regions and giant molecular clouds in the interacting Antennae Galaxy system: self-gravity only bound clouds above a certain mass threshold, and below this they must be bound by external pressure. Intriguingly, the pressure we find is comparable to that found by Heckman, Armus & Miley (1990) in the central few hundred parsecs of galaxies with starburst-driven superwinds. As such, the line ratios observed in the centre of NGC 6951 are consistent with an environment dominated by supernovae, perhaps indicative of a young post-starburst.

8 CONCLUSION

We have presented 3 mm interferometer data from the IRAM PdBI, which spatially resolves the HCN (1–0) and HCO$^+$ (1–0) molecular lines in the central few arcsecs of three nearby Seyfert galaxies: NGC 3079, NGC 6764, and NGC 5033. The main results of this study are as follows.

(i) For these galaxies, and also NGC 7469, we use a rotating disc model that takes into account beam smearing, to successfully match the observed line distribution and kinematics. The characteristics of NGC 5033 can be fitted by a thin disc having $\sigma/v < 0.1$. In contrast, NGC 7469, NGC 3079, and NGC 6764, all favour a thick disc with $\sigma/v > 0.3$. Combining these results with the earlier study of Sani et al. (2012), we find that in seven out of eight Seyferts, the HCN (1–0) line traces thick rather than thin discs in the central $\sim$100 pc.

(ii) The spectrum of NGC 3079 is dominated by numerous absorption lines, which are characterized by a double-peaked profile. The component closest to systemic is caused by absorption in the approaching side of the inner disc, which lies in front of a radio continuum knot in the north-west jet. Based on the depth of the H^{13}CN (1–0) feature [since H^{12}CN (1–0) is both saturated and blended with emission], we estimate the hydrogen column density in the disc to be $N_{\rm H} \sim 6 \times 10^{22}$ cm^{-2}. The other absorption component, with a broad blueshifted wing extending to -350 km s^{-1}, suggests the existence of a dense nuclear outflow. Correcting the HCN (1–0) and HCO$^+$ (1–0) lines for continuum absorption indicates that the emission lines are also partially self-absorbed.

(iii) We find a relation between HCN luminosity and dynamical mass. This implies either a relation between, or typical values for, the gas fraction and the conversion factor $\alpha_{\rm HCN}$ between HCN luminosity and gas mass. A gas fraction of $f_{\rm gas} \sim 0.1$ and $\alpha_{\rm HCN} \sim 10$ (consistent with the conclusion of Krips et al. 2008 from LVG calculations) can account for the observed relation.

(iv) An analysis of the HCN (1–0)/CO (2–1) and HCN (3–2)/HCN (1–0) line ratios in NGC 6951 indicates that the molecular gas is not in self-gravitating clouds. Instead, the clouds are likely to be pressure confined. The implied pressure of $P/k \sim 10^7$ cm^{-3} K is comparable to that measured in the centres of superwinds, suggesting that the ISM in the centre of NGC 6951 is consistent with an environment dominated by supernova.

ACKNOWLEDGEMENTS

REFERENCES

Aalto S. et al., 2015, A&A, 584, A42
Antonucci R., 1993, ARA&A, 31, 473
Bergin E., Tafalla M., 2007, ARA&A, 45, 339
Boger G., Sternberg A., 2005, ApJ, 632, 302
Braine J., Guélin M., Dumke M., Brouillet N., Herpin F., Wielebinski R., 1997, A&A, 326, 963
Burtscher L. et al., 2015, A&A, 578, 47
Cecil G., Bland-Hawthorn J., Veilleux S., Filippenko A. V., 2001, ApJ, 555, 338
Cecil G., Bland-Hawthorn J., Veilleux S., 2002, ApJ, 576, 745
Cid Fernandes R. et al., 2004, ApJ, 605, 105
Combes F. et al., 2013, A&A, 558, A124
Costagliola F. et al., 2011, A&A, 528, A30
Davies R. I., Tacconi L. J., Genzel R., 2004, ApJ, 602, 148
Davies R. I., Müller Sánchez F., Genzel R., Tacconi L. J., Hicks E. K. S., Friedrich S., Sternberg A., 2007, ApJ, 671, 1388
Davies R. et al., 2011, ApJ, 741, 69
Davies R., Mark D., Sternberg A., 2012, A&A, 537, A133
Downes D., Genzel R., Hjalmarson A., Nyman L. A., Ronnang B., 1982, ApJ, 252, L29
Downes D., Solomon P. M., Radford S. J. E., 1993, ApJ, 414, L13
Elitzur M., Shlosman I., 2006, ApJ, 648, L101
Engel H., Davies R., Genzel R., Taccconi L., Sturm E., Downes D., 2011, ApJ, 729, 58
Esquej P. et al., 2014, ApJ, 780, 86
Feltre A., Hatziminaoglou E., Fritz J., Franceschini A., 2012, MNRAS, 426, 120
Fritz J., Franceschini A., Hatziminaoglou E., 2006, MNRAS, 366, 767
Gao Y., Solomon P. M., 2004, ApJS, 152, 63
Gao Y., Carilli C. L., Solomon P. M., Vanden Bout P. A., 2007, ApJ, 660, L93
Garciá-Burillo S. et al., 2014, A&A, 567, A125
Goldsmith P., 2001, ApJ, 557, 736
Gottlieb C., Gottlieb E., Thaddeus P., 1983, ApJ, 264, 740
Granato G. L., Danese L., 1994, MNRAS, 268, 235
Granato G. L., Danese L., Franceschini A., 1997, ApJ, 486, 147
Hagiwara Y., Klöckner H.-R., Baan W., 2004, MNRAS, 353, 1055
Hailey-Dunsheath S. et al., 2012, ApJ, 755, 57
Harada N., Herbst E., Wakelam V., 2010, ApJ, 721, 1570
Hawarden T., Israel F., Geballe T., Wade R., 1995, MNRAS, 276, 1197
Heckman T., Armus L., Miley G., 1990, ApJSS, 74, 833
Hicks E. K. S., Davies R. I., Malkan M. A., Genzel R., Tacconi L. J., Müüller Sánchez F., Sternberg A., 2009, ApJ, 696, 448
Hicks E. K. S., Davies R. I., Maciejewski W., Emsellem E., Malkan M., Dumas G., Müüller-Sáánchez F., Rivers A., 2013, ApJ, 768, 107
Hönig S., Beckert T., Ohnaka K., Weigelt G., 2006, A&A, 452, 459
Hopkins P. F., Hayward C. C., Narayanan D., Hernquist L., 2012, MNRAS, 420, 320
Hota A., Saikia D., 2006, MNRAS, 371, 945
Hsieh P.-Y., Ho P., Kohno K., Hwang C.-Y., Matsushita S., 2012, ApJ, 747, 90
Huchra J., Geller M., Corwin H., 1995 ApJS, 99, 391
Iyomoto N., Fukazawa Y., Nakai N., Ishihara Y., 2001, ApJ, 561, L69
Kharb P., Hota A., Croston J. H., Hardcastle M. J., O'Dea C. P., Kraft R. P., Axon D. J., Robinson A., 2010, ApJ, 723, 580
Klaas U., Walker H., 2002, A&A, 391, 911
Klaassen P. D., Wilson C. D., 2007, ApJ, 663, 1092
Koda J., Sofue Y., Kohno K., Nakanishi H., Onodera S., Okumura S. K., Irwin J. A., 2002, ApJ, 573, 105
Kohno K., 2005, in Hüüttemeister S., Manthey E., Bomans D., Weis K., eds, AIP Conf. Proc. Vol. 783, The Evolution of Starbursts: The 331st Wilhelm and Else Heraeus Seminar. Am. Inst. Phys., New York, p. 203
Kohno K., Vila-Vilaró B., Sakamoto S., Kawabe R., Ishizuki S., Matsushita S., 2003, PASJ, 55, 103
Kohno K., Nakanishi K., Tosaki T., Muraoka K., Miura R., Ezawa H., Kawabe R., 2008, Ap&SS, 313, 279
Kondratko P. T., Greenhill L. J., Moran J. M., 2005, ApJ, 618, 618
Krips M. et al., 2007, A&A, 468, L63
Krips M., Neri R., García-Burillo S., Martíín S., Combes F., Graciáá-Carpio J., Eckart A., 2008, ApJ, 677, 262
Krips M. et al., 2011, ApJ, 736, 37
Krolik J. H., Begelman M. C., 1988, ApJ, 329, 702

Kukula M., Pedlar A., Baum S., O'Dea C., 1995, MNRAS, 276, 1262

Leon S. et al., 2007, A&A, 473, 747

Lepp S., Dalgarno A., 1996, A&A, 306, L21

Maloney P., Hollenbach D., Tielens A., 1996, ApJ, 466, 561

Martín S., Aladro R., Martín-Pintado J., Mauersberger R., 2010, A&A, 522, A62

Martin-Pintado J., Bachiller R., Fuente A., 1992, A&A, 254, 315

Meijerink R., Spaans M., 2005, A&A, 436, 397

Meijerink R., Spaans M., Israel F. P., 2007, A&A, 461, 793

Middelberg E., Agudo I., Roy A., Krichbaum T., 2007, MNRAS, 377, 731

Milam S. N., Savage C., Brewster M. A., Ziurys L. M., Wyckoff S., 2005, ApJ, 634, 1126

Morganti R., 2012, Proc. Sci., Outflows, feedback, jets (review). SISSA, Treiste, PoS(Seyfert 2012)019

Morganti R., Holt J., Saripalli L., Oosterloo T., Tadhunter C., 2007, A&A, 476, 735

Morganti R., Oosterloo T., Oonk J., Frieswijk W., Tadhunter C., 2015, A&A, 580, 1

Muller S., Dinh-V-Trung, 2009, ApJ, 696, 176

Müller-Sánchez F., Davies R., Genzel R., Tacconi L., Eisenhauer F., Hicks E., Friedrich S., Sternberg A., 2009, ApJ, 691, 749

Müller-Sánchez F., Prieto M. A., Mezcua M., Davies R. I., Malkan M. A., Elitzur M., 2013, ApJ, 763, L1

Nenkova M., Ivezić Ž., Elitzur M., 2002, ApJ, 570, L9

Netzer H., 2015, ARA&A, 53, 365

Papadopoulos P. P., 2007, ApJ, 656, 792

Pérez-Torres M. A., Alberdi A., 2007, MNRAS, 379, 275

Pier E., Krolik J., 1992, ApJ, 401, 99

Rangwala N., Maloney P., Wilson C., Glenn J., Kamenetzky J., Spinoglio L., 2015, ApJ, 806, 17

Riffel R., Postoriza M., Rodríguez-Ardila A., Bonatto C., 2009 MNRAS, 400, 273

Sakamoto K. et al., 2009, ApJ, 700, L104

Sani E. et al., 2012, MNRAS, 424, 1963

Schartmann M., Meisenheimer K., Camenzind M., Wolf S., Henning T., 2005, A&A, 437, 861

Schartmann M., Meisenheimer K., Camenzind M., Wolf S., Tristram K., Henning T., 2008, A&A, 482, 67

Schartmann M., Wada K., Prieto M. A., Burkert A., Tristram K., 2014, MNRAS, 445, 3878

Schöier F. L., van der Tak F. F. S., van Dishoeck E. F., Black J. H., 2005, A&A, 432, 369

Schweitzer M. et al., 2008, ApJ, 679, 101

Sobolev V., 1957, Sov. Astron., 1, 678

Sofue Y., Rubin V., 2001, ARA&A, 39, 137

Solomon P. M., Vanden Bout P. A., 2005, ARA&A, 43, 677

Solomon P., Radford S., Downes D., 1990, ApJ, 348, 53

Sternberg A., Dalgarno A., 1995, ApJS, 99, 565

Stevens J., Gear W., 2000, MNRAS, 312, L5

Takamiya T., Sofue Y., 2002, ApJ, 576, L15

Thean A., Mundell C., Pdelar A., Nicholson R., 1997, MNRAS, 290, 15

Thompson T. A., Quataert E., Murray N., 2005, ApJ, 630, 167

Tristram K. R. W., Burtscher L., Jaffe W., Meisenheimer K., Höönig S. F., Kishimoto M., Schartmann M., Weigelt G., 2014, A&A, 563, AA82

Trotter A. S., Greenhill L. J., Moran J. M., Reid M. J., Irwin J. A., Lo K.-Y., 1998, ApJ, 495, 740

Urry C. M., Padovani P., 1995, PASP, 107, 803

Usero A., García-Burillo S., Fuente A., Martín-Pintado J., Rodríguez-Fernández N., 2004, A&A, 419, 897

Veilleux S., Cecil G., Bland-Hawthorn J., Tully R. B., Filippenko A. V., Sargent W. L. W., 1994, ApJ, 433, 48

Viti S. et al., 2014, A&A, 570, A28

Vollmer B., Beckert T., Davies R., 2008, A&A, 491, 441

Wada K., 2012, ApJ, 758, 66

Wada K., Norman C. A., 2002, ApJ, 566, L21

Wada K., Papadopoulos P., Spaan M., 2009, ApJ, 702, 63

White R., Becker R., Helfand D., Gregg M., 1997, ApJ, 475, 479

Wiklind T., Combes F., 1995, A&A, 299, 382

Yamagishi M., Kandea H., Ishihara D., Komugi S., Suzuki T., Onaka T., 2010, PASJ, 62, 1085

Zaragoza-Cardiel J., Font J., Beckman J., García-Lorenzo B., Erroz-Ferrer S., Gutiérrez L., 2014 MNRAS, 445, 1412

Ziurys L. M., Snell R. L., Dickman R. L., 1989a, ApJ, 341, 857

Ziurys L. M., Friberg P., Irvine W. M., 1989b, ApJ, 343, 201

This paper has been typeset from a TEX/LATEX file prepared by the author.